Presynaptic NMDA receptors facilitate short-term plasticity and BDNF release at hippocampal mossy fiber synapses

Pablo J. Lituma[1], Hyung-Bae Kwon[1,4], Karina Alviña[1,5], Rafael Lujan[3], Pablo E. Castillo[1,2]*

[1] Dominick P. Purpura Department of Neuroscience, Albert Einstein College of Medicine, Bronx, NY 10461, U.S.A.
[2] Department of Psychiatry and Behavioral Sciences, Albert Einstein College of Medicine, Bronx, NY 10461, U.S.A.
[3] Instituto de Investigación en Discapacidades Neurológicas (IDINE), Facultad de Medicina, Universidad Castilla-La Mancha, 02008 Albacete, Spain.
[4] Present address: The Solomon H. Snyder Department of Neuroscience, John Hopkins University, School of Medicine, Baltimore, MD 21205, U.S.A.
[5] Present address: Department of Neuroscience, University of Florida, 1149 Newell Drive, Room L1-100, Gainesville, FL, 32611, U.S.A.

Running title: Role of presynaptic NMDA receptors in short-term plasticity

Keywords: CA3, ionotropic, hippocampus, presynaptic calcium, autoreceptors

* To whom correspondence should be addressed:

Pablo E. Castillo, MD/PhD
Dominick P. Purpura Department of Neuroscience
Albert Einstein College of Medicine
1410 Pelham Parkway South
Kennedy Center, Room 703
Bronx, NY 10461, USA
Email: pablo.castillo@einsteinmed.org

Funding sources: This work supported by the NIH (F31-MH109267 to PJL; R01 MH116673, R01MH125772, and R01 NS 113600 to P.E.C.) and by the Spanish Ministerio de Economia y Competitividad (RTI2018-095812-B-I00) and Junta de Comunidades de Castillo-La Mancha (SBPLY/17/180501/000229) to RL.

Acknowledgements: We thank all the Castillo lab members for invaluable discussions. We also thank Dr. Hyungju Park for his generous gift of the BDNF-phluorin DNA construct, Dr. Michael Higley for sharing *Grin1* floxed mice, and Dr. Pascal Kaeser for his generous gift of the Cre-dependent ChIEF DNA construct.

Title: 112 characters (with spaces)
Summary: 138 words, 1080 characters with spaces
Main text (excluding Summary, Methods, references and figure legends): 4,490
Figures: 8
Supplementary figures: 12

Summary

Neurotransmitter release is a highly controlled process by which synapses can critically regulate information transfer within neural circuits. While presynaptic receptors –typically activated by neurotransmitters and modulated by neuromodulators– provide a powerful way of fine-tuning synaptic function, their contribution to activity-dependent changes in transmitter release remains poorly understood. Here, we report that presynaptic NMDA receptors (preNMDARs) at mossy fiber boutons in the rodent hippocampus can be activated by physiologically relevant patterns of activity and selectively enhance short-term synaptic plasticity at mossy fiber inputs onto CA3 pyramidal cells and mossy cells, but not onto inhibitory interneurons. Moreover, preNMDARs facilitate brain-derived neurotrophic factor (BDNF) release and contribute to presynaptic calcium rise. Taken together, our results indicate that by increasing presynaptic calcium, preNMDARs fine tune mossy fiber neurotransmission and can control information transfer during dentate granule cell burst activity that normally occur *in vivo*.

Introduction

Neurotransmission is a dynamic and highly regulated process. The activation of ionotropic and metabotropic presynaptic autoreceptors provides a powerful way of fine-tuning neurotransmission via the facilitation or inhibition of neurotransmitter release (Burke & Bender, 2019; Engelman & MacDermott, 2004; Miller, 1998; Pinheiro & Mulle, 2008; Schicker et al., 2008). Due to their unique functional properties, including high calcium-permeability, slow kinetics and well-characterized role as coincidence-detectors (Cull-Candy et al., 2001; Lau & Zukin, 2007; Paoletti et al., 2013; Traynelis et al., 2010), presynaptic NMDA receptors (preNMDARs) have received particular attention (Banerjee et al., 2016; Bouvier et al., 2015; Bouvier et al., 2018; Duguid, 2013; Duguid & Smart, 2009; Wong et al., 2020). Regulation of neurotransmitter release by NMDA autoreceptors in the brain was suggested three decades ago (Martin et al., 1991). Anatomical evidence for preNMDARs arose from an immuno-electron microscopy study revealing NMDARs at the mossy fiber giant bouton of the monkey hippocampus (Siegel et al., 1994), followed by functional studies in the entorhinal cortex indicating that preNMDARs tonically increase spontaneous glutamate release and also facilitate evoked release in a frequency-dependent manner (Berretta & Jones, 1996; Woodhall et al., 2001). Since these early studies, although evidence for preNMDARs has accumulated throughout the brain (Banerjee et al., 2016; Bouvier et al., 2018; Duguid & Smart, 2009), the presence and functional relevance of preNMDARs at key synapses in the brain have been called into question (Carter & Jahr, 2016; Duguid, 2013).

Mossy fibers (mf) – the axons of dentate granule cells (GCs) – establish excitatory synapses onto proximal dendrites of CA3 pyramidal neurons, thereby conveying a major excitatory input to the hippocampus proper (Amaral et al., 2007; Henze et al., 2000). This synapse displays

103 uniquely robust frequency facilitation both *in vitro* (Nicoll & Schmitz, 2005; Salin et al., 1996;
104 Vyleta et al., 2016) and *in vivo* (Hagena & Manahan-Vaughan, 2010; Vandael et al., 2020). The
105 molecular basis of this short-term plasticity is not fully understood but likely relies on diverse
106 presynaptic mechanisms that increase glutamate release (Jackman & Regehr, 2017; Rebola et
107 al., 2017). Short-term, use-dependent facilitation is believed to play a critical role in information
108 transfer, circuit dynamics and short-term memory (Abbott & Regehr, 2004; Jackman & Regehr,
109 2017; Klug et al., 2012). The mf-CA3 synapse can strongly drive the CA3 network during short
110 bursts of presynaptic activity (Chamberland et al., 2018; Henze et al., 2002; Vyleta et al., 2016;
111 Zucca et al., 2017), an effect that likely results from two key properties of this synapse, namely,
112 its strong frequency facilitation and proximal dendritic localization. In addition to CA3 pyramidal
113 neurons, mf axons establish synaptic connections with hilar mossy cells (MC) and inhibitory
114 interneurons (IN) (Amaral et al., 2007; Henze et al., 2000). These connections also display
115 robust short-term plasticity (Lysetskiy et al., 2005; Toth et al., 2000), which may contribute
116 significantly to information transfer and dynamic modulation of the dentate gyrus (DG)-CA3
117 circuit (Bischofberger et al., 2006; Evstratova & Toth, 2014; Lawrence & McBain, 2003). Despite
118 early evidence for preNMDARs at mf boutons (Siegel et al., 1994), whether these receptors
119 modulate neurotransmission at mf synapses is unknown. Intriguingly, mfs contain one of the
120 highest expression levels of brain-derived neurotrophic factor, BDNF (Conner et al., 1997).
121 While preNMDARs were implicated in BDNF release at corticostriatal synapses (Park et al.,
122 2014), whether putative preNMDARs impact BDNF release at mf synapses remains unexplored.
123
124 Here, to examine the potential presence and impact of preNMDARs at mf synapses, we utilized
125 multiple approaches, including immunoelectron microscopy, selective pharmacology for
126 NMDARs, a genetic knockout strategy to remove NMDARs from presynaptic GCs, two-photon
127 imaging of BDNF release, and presynaptic Ca^{2+} signals in acute rodent hippocampal slices. Our
128 findings indicate that preNMDARs contribute to mf short-term plasticity and promotes BDNF

129 release likely by increasing presynaptic Ca^{2+}. Thus, preNMDARs at mfs may facilitate
130 information transfer and provide an important point of regulation in the DG – CA3 circuit by
131 regulating both glutamate and BDNF release.
132
133 **Results**
134
135 **Electron microscopy reveals presynaptic NMDA receptors at mossy fiber terminals**
136 To determine the potential localization of NMDA receptors at the mf terminals of the rodent
137 hippocampus, we performed electron microscopy and post-embedding immunogold labeling in
138 rats using a validated antibody for the obligatory subunit GluN1 (Petralia et al., 1994; Siegel et
139 al., 1994; Takumi et al., 1999; Watanabe et al., 1998). Gold particles were detected in the main
140 body of the postsynaptic density as well as presynaptic mf terminals (**Figure 1A-C**). GluN1
141 localized in mf boutons in a relatively high proportion to the active zone, as compared to
142 associational-commissural (ac) synapse in the same CA3 pyramidal neuron (**Figure 1D**; mf,
143 ~32% presynaptic particles; ac, <10% presynaptic particles; n = 3 animals). Similar
144 quantification for AMPA receptors did not reveal presynaptic localization of these receptors in
145 either mf or associational commissural synapses (**Figure 1-figure supplement 1**; ~5%
146 presynaptic particles, n = 3 animals). Together, these results provide anatomical evidence for
147 preNMDARs at mf-CA3 synapses.
148
149 **Both NMDAR antagonism and genetic deletion from presynaptic granule cells reduce**
150 **mossy fiber low-frequency facilitation**
151 Presynaptic short-term plasticity, in the form of low-frequency (~1 Hz) facilitation (LFF), is
152 uniquely robust at the mf-CA3 synapse (Nicoll & Schmitz, 2005; Salin et al., 1996). To test a
153 potential involvement of preNMDARs in LFF, we monitored AMPAR-mediated excitatory
154 postsynaptic currents (EPSCs) from CA3 pyramidal neurons in acute rat hippocampal slices.

155 Neurons were held at V_h= -70 mV to minimize postsynaptic NMDAR conductance, and mfs were
156 focally stimulated with a bipolar electrode (theta glass pipette) placed in *stratum lucidum* ~100
157 μm from the recorded cell. LFF was induced by stepping the stimulation frequency from 0.1 Hz
158 to 1 Hz for ~2 min in the presence of picrotoxin (100 μM) to block fast inhibitory synaptic
159 transmission, and a low concentration of the AMPAR noncompetitive antagonist LY303070 (0.5
160 μM) to minimize CA3-CA3 recurrent activity (Kwon & Castillo, 2008). Bath-application of the
161 NMDAR irreversible open channel blocker MK-801 (50 μM) significantly reduced LFF (**Figure**
162 **1E**). In addition, the competitive NMDAR antagonists D-APV (100 μM) or R-CPP (50 μM)
163 yielded a comparable reduction of facilitation (**Figure 1F**). To confirm that these synaptic
164 responses were mediated by mfs, the mGluR2/3 agonist DCG-IV (1 μM) was applied at the end
165 of all recordings (Kamiya et al., 1996). To control for stability, we performed interleaved
166 experiments in the absence of NMDAR antagonists and found that LFF remained unchanged
167 (**Figure 1-figure supplement 2A**). These findings indicate NMDAR antagonism reduces mf-
168 CA3 short-term plasticity (LFF), suggesting that preNMDARs could contribute to this form of
169 presynaptic plasticity.
170
171 The reduction in facilitation of AMPAR-transmission could be due to dampening of CA3
172 recurrent activity by NMDAR antagonism (Henze et al., 2000; Kwon & Castillo, 2008; Nicoll &
173 Schmitz, 2005). To discard this possibility, we repeated our experiments in a much less
174 excitable network in which AMPAR-mediated synaptic transmission was selectively blocked by a
175 high concentration of the noncompetitive antagonist LY303070 (15 μM) and monitored the
176 kainate receptor (KAR)-mediated component of mf synaptic transmission (Castillo et al., 1997;
177 Kwon & Castillo, 2008). In addition, 2 mM MK-801 was included in the intracellular recording
178 solution to block postsynaptic NMDARs (Corlew et al., 2008) (**Figure 1-figure supplement 3**).
179 To further ensure postsynaptic NMDAR blockade, we voltage-clamped the CA3 pyramidal
180 neuron at -70 mV and waited until NMDAR-mediated transmission was eliminated and only

181 KAR-EPSCs remained. Under these recording conditions, bath-application of MK-801 (50 μM)
182 also reduced LFF of KAR-mediated transmission (**Figure 1G**), whereas LFF remained
183 unchanged in interleaved control experiments (**Figure 1-figure supplement 2B**). At the end of
184 these recordings**,** 10 μM NBQX was applied to confirm KAR-transmission (**Figure 1G; Figure 1-**
185 **figure supplement 2B**) (Castillo et al., 1997; Kwon & Castillo, 2008). It is therefore unlikely that
186 the reduction of LFF mediated by NMDAR antagonism could be explained by recurrent network
187 activity, suggesting a direct effect on transmitter release.
188
189 To further support a role of preNMDARs in mf LFF, we took a genetic approach by conditionally
190 removing NMDARs from GCs in *Grin1* floxed mice. To this end, an AAV5-CamKII-Cre-GFP virus
191 was bilaterally injected in the DG to selectively delete *Grin1* expression, whereas AAV5-CamKII-
192 eGFP was injected in littermates as a control at postnatal days 16-20 in both groups (**Figure**
193 **2A**). Two weeks after surgery, we prepared acute hippocampal slices and examined the efficacy
194 of *Grin1* deletion by analyzing NMDAR-mediated transmission in GFP^+ GCs of *Grin1*-cKO and
195 control mice. We confirmed that in contrast to control mice, no NMDAR-EPSCs were elicited by
196 electrically stimulating medial perforant path inputs in *Grin1*-cKO GCs voltage-clamped at +40
197 mV in the presence of 100 μM picrotoxin and 10 μM NBQX (**Figure 2B**). As expected, the
198 NMDAR/AMPAR ratio was significantly reduced in *Grin1*-cKO mice compared to control (**Figure**
199 **2C**). Only acute slices that exhibited robust GFP fluorescence in the DG were tested for LFF of
200 AMPAR-transmission in CA3. We found that LFF was significantly reduced in *Grin1*-cKOs as
201 compared to controls (**Figure 2D**), indicating that genetic removal of NMDARs from GCs
202 recapitulated NMDAR antagonism (**Figure 1E-G**). *Grin1* deletion did not affect basal transmitter
203 release as indicated by a comparable paired-pulse ratio to control (Control: 2.5 ± 0.36, n = 13
204 cells; *Grin1* cKO: 2.4 ± 0.31, n = 13 cells; U > 0.5, Mann-Whitney test). Collectively, our findings
205 using two distinct approaches strongly suggest that NMDAR activation in GCs increases LFF of
206 mf-CA3 synaptic transmission.

207

208 **Reduced facilitation by NMDAR antagonism is independent of the granule cell**
209 **somatodendritic compartment**

210 Bath application of MK-801 could have blocked dendritic NMDARs in GCs and potentially
211 affected transmitter release (Christie & Jahr, 2008; Duguid, 2013). To address this possibility,
212 we repeated our experiments after performing a surgical cut in the granular layer of the DG in
213 order to isolate mf axons from GCs (**Figure 3-figure supplement 1A**). Under these conditions,
214 MK-801 bath application still reduced LFF (**Figure 3A**), and LFF was stable in control, acutely
215 transected axons (**Figure 3B**). In addition, puffing D-APV (2 mM) in *stratum lucidum* near (~200
216 µm) the recorded neuron also reduced LFF (**Figure 3C**), whereas puffing ACSF had no effect
217 (**Figure 3D**). Lastly, in a set of control experiments, we confirmed that D-APV puffs were
218 sufficient to transiently block NMDAR-mediated transmission in CA3 but not in DG (**Figure 3-**
219 **figure supplement 1B,C**). Together, these results support the notion that LFF reduction was
220 due to the blockade of preNMDARs but not somatodendritic NMDARs on GCs.

221

222 **PreNMDARs boost information transfer by enhancing burst-induced facilitation at mossy**
223 **fiber synapses**

224 GCs *in vivo* typically fire in brief bursts (Diamantaki et al., 2016; GoodSmith et al., 2017; Henze
225 et al., 2002; Pernia-Andrade & Jonas, 2014; Senzai & Buzsaki, 2017). To test whether
226 preNMDARs contribute to synaptic facilitation that occurs during more physiological patterns of
227 activity, mfs were activated with brief bursts (5 stimuli, 25 Hz). We first took an optogenetic
228 approach and used a Cre-dependent ChIEF virus to selectively light-activate mf-CA3 synapses
229 in *Grin1*-cKO and control mice. Thus, animals were injected with a mix of AAV5-CamKII-CreGFP
230 + AAV-DJ-FLEX-ChIEF-tdTomato viruses in the DG (**Figure 4A**). At least four weeks after
231 surgery, acute slices were prepared and burst-induced facilitation of AMPAR-mediated
232 transmission in CA3 was assessed (**Figure 4B,C**). Burst-induced facilitation triggered by light

233 stimulation and measured as the ratio of EPSCs elicited by the 5th and 1st pulse (P5/P1 ratio),
234 was significantly reduced in *Grin1*-cKO animals as compared to controls. Because these bursts
235 of activity can activate the CA3 network (Henze et al., 2000; Kwon & Castillo, 2008; Nicoll &
236 Schmitz, 2005), we next monitored KAR-EPSCs under conditions of low excitability (as in Figure
237 1G). MK-801 bath application also reduced burst-induced facilitation, whereas facilitation
238 remained unchanged in naïve slices (**Figure 4D,E**). In a separate set of experiments, we
239 confirmed the reduction of MK-801 on burst-induced facilitation under more physiological
240 recording conditions (**Figure 4-figure supplement 1**). Lastly, we tested whether preNMDARs,
241 by facilitating glutamate release during bursting activity, could bring CA3 pyramidal neurons to
242 threshold and trigger postsynaptic action potentials. To test this possibility, we monitored action
243 potentials elicited by KAR-EPSPs (resting membrane potential -70 ± 2 mV) from CA3 pyramidal
244 neurons intracellularly loaded with 2 mM MK-801. Under these recording conditions, MK-801
245 bath application significantly reduced the mean number of spikes per burst (**Figure 4F**). No
246 changes in mean spikes per burst were observed in naïve slices over time (**Figure 4G**).
247 Application of 10 μM NBQX at the end of these experiments confirmed that action potentials
248 were induced by KAR-mediated synaptic responses. Consistent with these observations, MK-
249 801 also reduced the mean number of spikes per burst when AMPAR-mediated action
250 potentials were recorded from CA3 pyramidal neurons (**Figure 4-figure supplement 2**). In
251 control experiments, we found that intracellular MK-801 effectively blocked postsynaptic
252 NMDAR transmission during burst stimulation (**Figure 4-figure supplement 3**). Altogether,
253 these results indicate that preNMDARs at mf-CA3 synapses can contribute to information
254 transfer from the DG to CA3.
255
256
257 **PreNMDARs contribute to presynaptic calcium rise and can be activated by glutamate**
258 PreNMDARs could facilitate glutamate and BDNF release by increasing presynaptic Ca^{2+} rise

259 (Bouvier et al., 2016; Buchanan et al., 2012; Corlew et al., 2008; Park et al., 2014). To test this
260 possibility at mf-CA3 synapses, we combined a conditional knockout strategy with Ca^{2+} imaging
261 using two-photon laser scanning microscopy. We first deleted preNMDARs by injecting AAV5-
262 CamKII-mCherry-Cre virus in the DG of *Grin1* floxed mice, and littermate animals injected with
263 AAV5-CamKII-mCherry virus served as control (**Figure 5A**). Two weeks after surgery, we
264 confirmed the efficacy of *Grin1* deletion by activating medial perforant path inputs and
265 monitoring NMDAR/AMPAR ratios in GCs of control and *Grin1*-cKO animals (**Figure 5A**).
266 Virtually no NMDAR-EPSCs were detected at V_h= +40 mV in *Grin1*-cKO animals (**Figure 5A**).
267 Acute slices that exhibited robust mCherry fluorescence in the DG were used for Ca^{2+} imaging
268 experiments. To maximize our ability to detect preNMDAR-mediated Ca^{2+} signals, we used a
269 recording solution that contained 0 mM Mg^{2+}, 4 mM Ca^{2+} and 10 μM D-Serine (Carter & Jahr,
270 2016). GCs expressing mCherry were patch-loaded with 35 μM Alexa 594 (used as
271 morphological dye) and 200 μM Fluo-5F, and mf axons were imaged and followed towards CA3
272 until giant boutons (white arrows) were identified (**Figure 5B**). We found that Ca^{2+} transients
273 (CaTs) elicited by direct current injection in the GC soma (5 action potentials, 25 Hz) were
274 significantly smaller in *Grin1*-cKO animals as compared to control (**Figure 5C-E**). In addition,
275 NMDAR antagonism with D-APV reduced presynaptic Ca^{2+} rise even under more physiological
276 Mg^{+2} concentration in acute rat hippocampal slices (**Figure 5-figure supplement 1**). Thus,
277 preNMDARs contribute significantly to presynaptic Ca^{2+} rise in mf boutons, and by this means
278 likely facilitates synaptic transmission, although a potential contribution of Ca^{2+} rise-independent
279 effects cannot be discarded.
280
281 Lastly, we sought to determine if direct activation of preNMDARs could drive Ca^{2+} influx in mf
282 giant boutons. To test this possibility, we elicited CaTs by two-photon glutamate uncaging (2PU)
283 on mf boutons of control and *Grin1*-cKO animals (**Figure 6A**). As previously described,
284 mCherry GCs were patch-loaded with Alexa 594 and Fluo-5F in a recording solution designed to

285 maximize the detection of preNMDAR-mediated Ca^{2+} signals (as in Figure 5). We first
286 confirmed that glutamate 2PU-induced CaTs in dendritic spine heads of GCs were strongly
287 reduced in *Grin1*-cKO animals as compared to controls (**Figure 6B,C**). To verify that reduced
288 Ca^{2+} signals (ΔG/R) were a result of *Grin1* deletion and not differences in uncaging laser power,
289 we performed a laser power intensity–response curve, and found that *Grin1*-cKO animals
290 exhibited reduced ΔG/R signals as compared to control regardless of laser power intensity
291 (**Figure 6-figure supplement 1**). We next measured glutamate 2PU-induced CaTs in mf giant
292 boutons (identified as in Figure 5B) and found that single uncaging pulses were insufficient to
293 drive detectable CaTs in control boutons (**Figure 6-figure supplement 2**). However, a burst of
294 2PU stimulation (5 pulses, 25 Hz) induced CaTs in mf boutons of control but not in *Grin1*-cKO
295 animals (**Figure 6D,E**). Additionally, CaTs elicited by 2PU stimulation were abolished by D-APV
296 application (**Figure 6-figure supplement 3**). These findings indicate that brief bursts of
297 glutamate 2PU, a manipulation that mimics endogenous release of glutamate during
298 physiological patterns of activity, induces presynaptic Ca^{2+} influx in mf boutons by activating
299 preNMDARs.
300

301 **PreNMDARs promote BDNF release from mossy fiber boutons**

302 Previous work implicated preNMDARs in the release of BDNF at corticostriatal synapses
303 following burst stimulation and presynaptic Ca^{2+} elevations (Park et al., 2014). Given the high
304 expression levels of BDNF in mfs (Conner et al., 1997; Yan et al., 1997), we examined the
305 potential role for preNMDARs in BDNF release from mf terminals. To this end, a Cre-dependent
306 BDNF reporter (BDNF-pHluorin) was injected in *Grin1*-floxed and control animals. Littermate
307 mice were injected with a mix of AAV5-CamKII-mCherry-Cre + AAV-DJ-DIO-BDNF-pHluorin
308 viruses in the DG (**Figure 7A**). At least four weeks after surgery, acute slices were prepared for
309 two-photon laser microscopy to image mf boutons. After acquiring a stable baseline of BDNF-
310 pHluorin signals, mfs were repetitively activated (see Methods) (**Figure 7B**). BDNF-pHluorin

311 signals were analyzed by measuring ΔF/F, where ΔF/F reductions indicate BDNF release (Park
312 et al., 2014). We found that GluN1-deficient mf boutons showed a significant (~50%)
313 impairment in BDNF release as compared to control (**Figure 7C-D**). Furthermore, using a more
314 physiological pattern of burst stimulation, GluN1-lacking mf boutons still displayed altered BDNF
315 release as compared to control (**Figure 7-figure supplement 1**). Taken together, our results
316 suggest preNMDARs contribute significantly to BDNF release during repetitive or burst
317 stimulation of mf synapses.
318
319 **PreNMDAR-mediated regulation of mossy fiber synapses is input-specific**
320 In addition to providing a major excitatory input to the hippocampus proper, mf axons also
321 synapse onto excitatory hilar mossy cells and inhibitory neurons in CA3 (Amaral et al., 2007;
322 Henze et al., 2000; Lawrence & McBain, 2003). To test whether preNMDARs could also play a
323 role at these synapses, we visually patched mossy cells and interneurons in acute rat
324 hippocampal slices, loaded them with 35 μM Alexa 594 (**Figure 8A**) and 2 mM MK-801, and
325 monitored AMPAR-EPSCs (V_h = -70 mV). Unlike mf-CA3 synapses, mf synapses onto CA3
326 interneurons in *stratum lucidum* do not express LFF, but can undergo burst-induced facilitation
327 or depression (Toth et al., 2000). We found that MK-801 bath application had no effect on burst-
328 induced facilitation or depression (**Figure 8B**), suggesting preNMDARs do not play a role at mf-
329 Interneuron synapses in CA3. Mf inputs onto hilar mossy cells undergo robust activity-
330 dependent facilitation (Lysetskiy et al., 2005). Similar to mf-CA3 synapses, we found that MK-
331 801 reduced LFF (**Figure 8C**). Stability experiments of mf transmission at CA3 interneurons or
332 hilar mossy cells showed no significant differences (**Figure 8-figure supplement 1**). Taken
333 together, our findings demonstrate that preNMDARs facilitate mf transmission onto excitatory
334 neurons but not onto inhibitory interneurons.
335
336

Discussion

In this study, we provide evidence that hippocampal mf boutons express preNMDARs whose activation fine-tunes mf synaptic function. Specifically, our results show that preNMDARs enhance mf short-term plasticity in a target cell-specific manner. By enhancing glutamate release onto excitatory but not inhibitory interneurons, preNMDARs increase GC-CA3 spike transfer. Moreover, using two-photon Ca^{2+} imaging, we demonstrate that preNMDARs contribute to presynaptic Ca^{2+} rise in mf boutons. Lastly, upon repetitive activity, preNMDARs promote BDNF release from mf boutons. Taken together, our findings indicate that preNMDARs act as autoreceptors to boost both glutamate and BDNF release at mf synapses. By regulating information flow in the DG-CA3 circuit, preNMDARs may play a significant role in learning and memory.

Early studies using immunoperoxidase electron microscopy revealed NMDARs in presynaptic compartments in multiple brain areas (for a review, see Corlew et al., 2008). Subsequent studies that used immunogold electron microscopy, a more precise localization method, identified NMDARs on the presynaptic membrane in a number of brain structures, including neocortex (Fujisawa & Aoki, 2003; Larsen et al., 2011), hippocampus (Berg et al., 2013; Jourdain et al., 2007; McGuinness et al., 2010), and amygdala (Pickel et al., 2006). In agreement with these studies, and using a previously validated antibody (Siegel et al., 1994), we identified prominent presynaptic labeling of the obligatory subunit GluN1 in mf boutons (Figure 1A-D). Moreover, we found that these receptors are close to the active zone and therefore well positioned to modulate neurotransmitter release.

Previous work in the cerebellum and neocortex suggested that somatodendritic potentials generated by NMDARs could signal to nerve terminals and lead to presynaptic Ca^{2+} elevations

363 (Christie & Jahr, 2008, 2009). Thus, changes in neurotransmitter release resulting from NMDAR
364 antagonism could be due to somatodendritic NMDARs but not necessarily preNMDARs residing
365 on nerve terminals (Duguid, 2013). However, we showed that focal NMDAR antagonism far
366 from the somatodendritic compartment and in transected axons still reduced short-term
367 plasticity at mf synapses (Figure 3), making it extremely unlikely that somatodendritic NMDARs
368 could explain our results. In further support of functional preNMDARs at mf boutons, we found
369 that 2PU of glutamate induced Ca^{2+} rise in control but not in GluN1-deficient boutons. Together,
370 our findings strongly support the presence of functional preNMDARs facilitating
371 neurotransmission at mf-CA3 synapses.
372
373 There is evidence that preNMDARs can operate as coincidence detectors at some synapses
374 (Duguid, 2013; Wong et al., 2020). At the mf-CA3 synapse, we found that preNMDARs
375 contribute to LFF (i.e. 1s inter-stimulus interval). This observation is intriguing given that the
376 presynaptic AP-mediated depolarization is likely absent by the time glutamate binds to
377 preNMDARs. However, coincidence detection may not be an essential requirement for mf
378 preNMDARs to modulate glutamate release. Of note, at resting membrane potential the
379 NMDAR conductance is not zero and the driving force for Ca^{2+} influx is high (Paoletti et al.,
380 2013; Traynelis et al., 2010). It is also conceivable that mf preNMDARs exhibit low-voltage
381 dependence, as it has been reported at other synapses (Wong et al., 2020). Remarkably, the
382 somatodendritic compartment of GCs can generate sub-threshold depolarizations at mf
383 terminals (a.k.a. excitatory presynaptic potentials) (Alle & Geiger, 2006). By alleviating the
384 magnesium blockade, these potentials might reduce the need for coincidence detection and
385 transiently boost the functional impact of mf preNMDARs.
386
387 While the presence of preNMDARs is downregulated during development both in neocortex
388 (Corlew et al., 2007; Larsen et al., 2011) and hippocampus (Mameli et al., 2005), we were able

389 to detect functional preNMDARs in young adult rats (P17-P28) and mice (P30-P44), once mf
390 connections are fully developed (Amaral & Dent, 1981). Functional preNMDARs have been
391 identified in axonal growth cones of hippocampal and neocortical neurons, suggesting these
392 receptors are important for regulating early synapse formation (Gill et al., 2015; Wang et al.,
393 2011). Because GCs undergo adult neurogenesis, and adult born GCs establish new
394 connections in the mature brain, preNMDARs could also play an important role at immature mf
395 synapses and functional integration of new born GCs into the mature hippocampus (Toni &
396 Schinder, 2015). Moreover, experience can modulate the expression and composition of
397 preNMDARs in neocortex (Larsen et al., 2014), a possibility not investigated in our study.
398
399 The glutamate that activates preNMDARs may originate from the presynaptic terminal, the
400 postsynaptic cell, nearby synapses or neighboring glial cells. Our results indicate that activation
401 of preNMDARs at mf synapses requires activity-dependent release of glutamate that likely
402 arises from mf boutons, although other sources cannot be discarded, including astrocytes. For
403 instance, at medial entorhinal inputs to GCs, preNMDARs appear to be localized away from the
404 presynaptic release sites and facing astrocytes, consistent with preNMDAR activation by
405 gliotransmitters (Jourdain et al., 2007; Savtchouk et al., 2019). In contrast, at mf-CA3 synapses
406 we found that preNMDARs are adjacent to the release sites suggesting a direct control on
407 glutamate release from mf boutons.
408
409 The precise mechanism by which preNMDARs facilitate neurotransmitter release is poorly
410 understood but it may include Ca^{2+} influx through the receptor and depolarization of the
411 presynaptic terminal with subsequent activation of voltage-gated Ca^{2+} channels (Banerjee et al.,
412 2016; Corlew et al., 2008). In support of this mechanism is the high Ca^{2+} permeability of
413 NMDARs (Paoletti et al., 2013; Rogers & Dani, 1995). Besides, presynaptic subthreshold
414 depolarization and subsequent activation of presynaptic voltage-gated Ca^{2+} channels is a

415 common mechanism by which presynaptic ionotropic receptors facilitate neurotransmitter
416 release (Engelman & MacDermott, 2004; Pinheiro & Mulle, 2008). PreNMDARs may also act in
417 a metabotropic manner (Dore et al., 2016) and facilitate spontaneous transmitter release
418 independent of Ca^{2+}-influx (Abrahamsson et al., 2017). Our findings demonstrating that the
419 open channel blocker MK-801 robustly reduced short-term plasticity at mf synapses support an
420 ionotropic mechanism that involves Ca^{2+} influx through preNMDARs. A previous study failed to
421 observe Ca^{+2} reductions in mf boutons by DL-APV (Liang et al., 2002). A combination of factors
422 could account for this discrepancy with our study, including a stronger mf repetitive stimulation
423 (20 pulses, 100 Hz) which may overcome a less potent NMDAR antagonism and/or the need for
424 preNMDAR activity, as well as the use of a higher affinity Ca^{2+} indicator (Fura-2 AM) and a lower
425 spatiotemporal resolution imaging approach. Nevertheless, in line with previous studies that
426 detected presynaptic Ca^{2+} rises following local activation of NMDARs (e.g. NMDA or glutamate
427 uncaging) in visual cortex (Buchanan et al., 2012) and cerebellum (Rossi et al., 2012), we
428 provide direct evidence that preNMDAR activation either by repetitive activation of mfs or 2PU
429 of glutamate increases presynaptic Ca^{2+} (Figures 5 and 6). Although the Ca^{2+} targets remain
430 unidentified, these may include proteins of the release machinery, calcium-dependent protein
431 kinases and phosphatases, and Ca^{2+} release from internal stores (Banerjee et al., 2016). In
432 addition to facilitating evoked neurotransmitter release, preNMDARs can promote spontaneous
433 neurotransmitter release as indicated by changes in miniature, action potential-independent
434 activity (e.g. mEPSCs) (for recent reviews, see Banerjee et al., 2016; Kunz et al., 2013; Wong et
435 al., 2020). A potential role for preNMDARs in spontaneous, action potential-independent release
436 at mf synapses cannot be discarded.
437
438 Our results show that activation of preNMDARs by physiologically relevant patterns of
439 presynaptic activity enhanced mf transmission and DG-CA3 information transfer (Figure 4). A
440 previous study reported NMDAR genetic deletion in GCs resulted in memory deficits (e.g.

441 pattern separation) (McHugh et al., 2007). Although the mechanism is unclear, it could involve
442 activity-dependent preNMDAR regulation of mf excitatory connections. We also found that
443 preNMDARs facilitate neurotransmitter release in a target cell-specific manner. Like in
444 neocortex (Larsen & Sjostrom, 2015), such specificity strongly suggests that preNMDARs have
445 distinct roles in controlling information flow in cortical microcircuits. Thus, preNMDAR facilitation
446 of mf synapses onto glutamatergic neurons but not GABAergic interneurons (Figure 8) may fine-
447 tune the CA3 circuit by increasing the excitatory/inhibitory balance.
448
449 Given the multiple signaling cascades known to regulate NMDARs (Lau & Zukin, 2007; Sanz-
450 Clemente et al., 2013), preNMDARs at mf synapses may provide an important site of
451 neuromodulatory control. PreNMDARs have been implicated in the induction of LTP and LTD at
452 excitatory or inhibitory synapses in several brain areas (Banerjee et al., 2016; Wong et al.,
453 2020). While most evidence, at least using robust induction protocols *in vitro,* indicates that
454 long-term forms of presynaptic plasticity at mf synapses can occur in the absence of NMDAR
455 activation (Castillo, 2012; Nicoll & Schmitz, 2005), our findings do not discard the possibility that
456 preNMDARs could play a role *in vivo* during subtle presynaptic activities. As previously reported
457 for corticostriatal LTP (Park et al., 2014), preNMDARs could regulate long-term synaptic
458 plasticity by controlling BDNF release, which is consistent with BDNF-TrkB signaling being
459 implicated in mf-CA3 LTP (Schildt et al., 2013). In addition, BDNF could facilitate glutamate
460 release by enhancing NMDAR function at the presynapse, as previously suggested (W. Chen et
461 al., 2014; Madara & Levine, 2008), although the precise mechanism(s) remain unclear. By
462 potentiating mf-CA3 transmission, BDNF could also promote epileptic activity (McNamara &
463 Scharfman, 2012). Lastly, dysregulation of NMDARs is commonly implicated in the
464 pathophysiology of brain disorders such as schizophrenia, autism, and epilepsy (Lau & Zukin,
465 2007; Paoletti et al., 2013). PreNMDAR expression and function have been suggested to be
466 altered in experimental models of disease, including neuropathic pain (Y. Chen et al., 2019;

Zeng et al., 2006), and epilepsy (Yang et al., 2006). At present, however, *in vivo* evidence for the involvement of preNMDARs in brain function and disease is rather indirect (Bouvier et al., 2015; Wong et al., 2020). The development of specific preNMDAR tools is required to determine the functional impact of these receptors *in vivo*.

Methods

Antibodies

A monoclonal antibody against GluN1 (clone 54.1 MAB363) was obtained from Millipore (Germany) and its specificity was characterized previously (Siegel et al., 1994). An affinity-purified polyclonal rabbit anti-GluA1-4 (pan-AMPA), corresponding to aa 724–781 of rat, was used and characterised previously (Nusser et al., 1998).

Immunohistochemistry for electron microscopy

Immunohistochemical reactions at the electron microscopic level were carried out using the post-embedding immunogold method as described earlier (Lujan et al., 1996). Briefly, animals (n = 3 rats were anesthetized by intraperitoneal injection of ketamine-xylazine 1 : 1 (0.1 mL/kg b.w.) and transcardially perfused with ice-cold fixative containing 4% paraformaldehyde, 0.1% glutaraldehyde and 15% saturated picric acid solution in 0.1 M phosphate buffer (PB) for 15 min. Vibratome sections 500 µm thick were placed into 1 M sucrose solution in 0.1 M PB for 2 h before they were slammed on a Leica EM CPC apparatus. Samples were dehydrated in methanol at -80°C and embedded by freeze-substitution (Leica EM AFS2) in Lowicryl HM 20 (Electron Microscopy Science, Hatfield, USA), followed by polymerization with UV light. Then, ultrathin 80-nm-thick sections from Lowicryl-embedded blocks of the hippocampus were picked

493 up on coated nickel grids and incubated on drops of a blocking solution consisting of 2% human
494 serum albumin in 0.05 M TBS and 0.03% Triton X-100. The grids were incubated with GluN1 or
495 pan-AMPA antibodies (10 µg/mL in 0.05 M TBS and 0.03% Triton X-100 with 2% human serum
496 albumin) at 28 °C overnight. The grids were incubated on drops of goat anti-rabbit IgG
497 conjugated to 10 nm colloidal gold particles (Nanoprobes Inc.) in 2% human serum albumin and
498 0.5% polyethylene glycol in 0.05 M TBS and 0.03% Triton X-100. The grids were then washed in
499 TBS and counterstained for electron microscopy with 1% aqueous uranyl acetate followed by
500 Reynolds's lead citrate. Ultrastructural analyses were performed in a JEOL-1010 electron
501 microscope.
502
503 **Hippocampal slice preparation**
504 Animal handling followed an approved protocol by the Albert Einstein College of Medicine
505 Institutional Animal Care and Use Committee in accordance with the National Institute of Health
506 guidelines. Acute rat hippocampal slices (400 µm thick) were obtained from Sprague-Dawley
507 rats, from postnatal day 17 (P17) to P28 of either sex. For procedures regarding transgenic
508 mouse slice preparation, see below. The hippocampi were isolated and cut using a VT1200s
509 microslicer (Leica Microsystems Co.) in a solution containing (in mM): 215 sucrose, 2.5 KCl, 26
510 $NaHCO_3$, 1.6 NaH_2PO_4, 1 $CaCl_2$, 4 $MgCl_2$, 4 $MgSO_4$ and 20 glucose. Acute slices were placed
511 in a chamber containing a 1:1 mix of sucrose cutting solution and normal extracellular artificial
512 cerebrospinal fluid (ACSF) recording solution containing (in mM): 124 NaCl, 2.5 KCl, 26
513 $NaHCO_3$, 1 NaH_2PO_4, 2.5 $CaCl_2$, 1.3 $MgSO_4$ and 10 glucose incubated in a warm-water bath at
514 33-34 ºC. The chamber was brought to room temperature for at least 15 min post-sectioning
515 and the 1:1 sucrose-ACSF solution was replaced by ACSF. All solutions were equilibrated with
516 95% O_2 and 5% CO_2 (pH 7.4). Slices were allowed to recover for at least 45 min in the ACSF
517 solution before recording. For physiological Mg^{+2} and Ca^{+2} experiments, ACSF solutions were
518 adjusted to (in mM): 1.2 $MgSO_4$, and 1.2 $CaCl_2$ and temperature was maintained at 35 ± 0.1 °C

519 in the submersion-type recording chamber heated by a temperature controller (TC-344B Dual
520 Automatic Temperature Controller, Warner Instruments).
521
522 **Electrophysiology**
523 Electrophysiological recordings were performed at 26.0 ± 0.1 ºC (unless otherwise stated) in a
524 submersion-type recording chamber perfused at 2 mL/min with normal ACSF supplemented
525 with the $GABA_A$ receptor antagonist picrotoxin (100 μM) and the selective AMPA receptor
526 (AMPAR) antagonist LY303070 at a low concentration (0.5 μM) to minimize CA3-CA3 recurrent
527 activity, or at a high concentration (15 μM) to isolate KAR-EPSCs and KAR-EPSPs to assess
528 monosynaptic mf transmission. Whole-cell recordings were made from CA3 pyramidal cells
529 voltage clamped at -70 mV using patch-type pipette electrodes (3-4 mΩ) containing (in mM):
530 131 cesium gluconate, 8 NaCl, 1 $CaCl_2$, 10 EGTA, 10 glucose, 10 HEPES, and 2 MK-801 pH
531 7.25 (280-285 mOsm) unless specified otherwise. KOH was used to adjust pH. Series
532 resistance (8-15 MΩ) was monitored throughout all experiments with a -5 mV, 80 ms voltage
533 step, and cells that exhibited a series resistance change (>20%) were excluded from analysis.
534 A stimulating bipolar electrode (theta glass, Warner Instruments) was filled with ACSF and
535 placed in *stratum lucidum* to selectively activate mfs using a DS2A Isolated Voltage Stimulator
536 (Digitimer Ltd.) with a 100 μs pulse width duration. AMPAR-EPSCs were recorded for a
537 baseline period of two minutes and low-frequency facilitation (LFF) was induced by stepping the
538 stimulation frequency from 0.1 to 1 Hz for two minutes. Facilitation was measured by taking a
539 ratio of the mean EPSC during the steady-state, LFF period of activity and the two-minute
540 baseline ($EPSC_{1Hz}/EPSC_{0.1Hz}$) before and after bath-application of NMDAR antagonists.
541
542 To qualify for analysis, mf responses met three criteria: 1) The 20-80% rise time of the AMPAR-
543 EPSC was less than 1 ms, 2) LFF was greater than 150%, 3) The AMPAR-EPSC displayed at
544 least 70% sensitivity to the group 2/3 mGluR agonist, DCG-IV (1 μM). Isolated KAR-EPSCs

545 were elicited by 2 pulses with a 5 ms inter-stimulus-interval for LFF experiments. Baseline
546 measurements were acquired at least 10 min after "break-in" to achieve optimal intracellular
547 blockade of postsynaptic NMDARs by MK-801 (2 mM) in the patch-pipette. To transect mf
548 axons in acute slices, a 45˚ ophthalmic knife (Alcon Surgical) was used to make a diagonal cut
549 across the hilus from the dorsal to ventral blades of the DG, and the subregion CA3b was
550 targeted for patch-clamp recordings. For D-APV (2 mM) puff experiments, a puffer device
551 (Toohey Company) was set to deliver 2-3 puffs of 100 ms duration at 3-4 psi during the two
552 minutes of LFF activity. The puffer pipette was placed at least 200 μm away from the recording
553 site and both the puff pipette and hippocampal slice were positioned to follow the direction of the
554 laminar perfusion flow in a low profile, submersion-type chamber (RC-26GLP, Warner
555 Instruments). Burst-induced facilitation was elicited by 5 pulses at 25 Hz with a 0.03 Hz inter-
556 trial-interval for a baseline period of 10 min. Facilitation was measured by calculating the ratio of
557 the mean KAR-EPSC peak of the 5th pulse to the 1st pulse (P_5/P_1) before and after bath-
558 application of MK-801 (50 μM). To study KAR induced action potentials, CA3 pyramidal cells
559 were whole-cell patch-clamped with internal solution containing in (mM): 112 potassium
560 gluconate, 17 KCl, 0.04 $CaCl_2$, 0.1 EGTA, 10 HEPES, 10 NaCl, 2 MgATP, 0.2 Na_3GTP and 2
561 MK-801, pH 7.2 (280-285 mOsm). Current-clamped CA3 cells were held at -70 mV during burst
562 stimulation of mfs (5 pulses at 25 Hz) to monitor evoked action potentials. Spike-transfer was
563 measured by quantifying mean number of spikes/burst for a 10 min period before and after bath
564 application of MK-801 (50 μM). Robust sensitivity to the AMPAR/KAR selective antagonist
565 NBQX (10 μM) confirmed KAR-EPSC responses. Similarly, CA3 pyramidal cells were kept in
566 current-clamp mode for AMPAR-mediated action potential monitoring in the presence of
567 LY303070 (0.5 μM) and picrotoxin (100 μM). AMPAR-mediated mf action potentials were
568 confirmed by blockade of responses following application of DCG-IV (1 μM). Both hilar mossy
569 cells and CA3 interneurons were visually patched-loaded with Alexa 594 (35 μM) and
570 morphological identity was confirmed by two-photon laser scanning imaging at the end of

experiments. Hilar mossy cells were voltage clamped at -70 mV and a bipolar electrode was placed in the DG to activate mf inputs. The data analysis and inclusion criteria used for mf experiments (described above) was also implemented for hilar mossy cell recordings. CA3 interneurons were voltage clamped at -70 mV and burst-stimulated, facilitation was assessed as previously mentioned. Both facilitating and depressing mf responses were included for analysis given the diversity of mf-CA3 interneuron transmission (Toth et al., 2000). Whole-cell voltage and current clamp recordings were performed using an Axon MultiClamp 700B amplifier (Molecular Devices). Signals were filtered at 2 kHz and digitized at 5 kHz. Stimulation and acquisition were controlled with custom software (Igor Pro 7).

Transgenic animals

Grin1-floxed littermate mice of either sex (P16-20) were injected with 1 µL of AAV5-CamKII-eGFP, AAV5-CamKII-CreGFP, AAV5-CamKII-mCherry, or AAV5-CamKII-mCherry-Cre viruses at a rate of 0.12 µL/min at coordinates (-1.9 mm A/P, 1.1 mm M/L, 2.4 mm D/V) targeting the DG using a stereotaxic apparatus (Kopf Instruments). Two weeks post-surgery mice were sacrificed for electrophysiology or Ca^{2+} imaging experiments. Mice were transcardially perfused with 20 mL of cold NMDG solution containing in (mM): 93 NMDG, 2.5 KCl, 1.25 NaH_2PO_4, 30 $NaHCO_3$, 20 HEPES, 25 glucose, 5 sodium ascorbate, 2 Thiourea, 3 sodium pyruvate, 10 $MgCl_2$, 0.5 $CaCl_2$, brought to pH 7.35 with HCl. The hippocampi were isolated and cut using a VT1200s microslicer in cold NMDG solution. Acute mouse slices were placed in an incubation chamber containing normal ACSF solution that was kept in a warm water bath at 33-34 ˚C. All solutions were equilibrated with 95% O_2 and 5% CO_2 (pH 7.4). Post-sectioning, slices recovered at room temperature for at least 45 min prior to experiments. For NMDAR/AMPAR ratios, GCs were patch-clamped with the cesium internal solution previously mentioned containing either Alexa 594 (35 µM) for GFP^+ cells (laser tuned to 830 nm/910 nm, respectively) or Alexa 488 (35 µM) for $mCherry^+$ cells (laser tuned to 910 nm/780 nm, respectively). AMPAR-

EPSCs were recorded at -65 mV in the presence of picrotoxin (100 μM) by placing a bipolar electrode near the medial perforant path and delivering a 100 μs pulse width duration using an Isoflex stimulating unit. AMPAR-EPSCs were acquired for at least 5 min followed by bath-application of NBQX (10 μM) to isolate NMDAR-EPSCs. GCs were brought to +40 mV to alleviate magnesium block and record optimal NMDAR-EPSCs. NMDAR/AMPAR ratios were measured by taking the mean NMDAR-EPSC/AMPAR-EPSC for a 5 min period of each component. Only acute mouse slices with optimal GFP and mCherry reporter fluorescence (i.e. robust expression, ≥ 75% of dentate gyrus fluorescence) were used for electrophysiology, and Ca^{2+} and BDNF imaging experiments. *Grin1*-floxed animals (The Jackson Laboratory) were kindly provided by Dr. Michael Higley (Yale University).

Optogenetics

Grin1 floxed and control mice of either sexes (P17-20) were injected with a 1:2 mix of AAV5-CamKII-CreGFP/AAV-DJ-FLEX-ChIEF-tdTomato viruses targeting the DG, using the same coordinates described above. At least four weeks post-surgery acute hippocampal slices were prepared as previously described and slices showing optimal GFP and tdTomato expression were used for electrophysiology experiments. Mf optical burst-stimulation was elicited by using a Coherent 473 nm laser (4-8 mW) delivering 5 pulses at 25 Hz with a 1-2 ms pulse width duration. Facilitation was measured by taking a ratio of the mean AMPAR-EPSC peak of the 5th pulse to the 1st pulse (P_5/P_1) in control and *Grin1*-cKO animals.

Two-photon calcium imaging and MNI-glutamate uncaging

mCherry+ GCs were patch-loaded with an internal solution containing in (mM): 130 $KMeSO_4$, 10 HEPES, 4 $MgCl_2$, 4 Na_2ATP, 0.4 NaGTP, 10 sodium phosphocreatine, 0.035 Alexa 594 (red morphological dye), and 0.2 Fluo-5F (green calcium indicator), 280-285 mOsm. KOH was used to adjust pH. GCs near the hilar border were avoided and GCs that exhibited adult-born GCs

electrophysiological properties were excluded from analysis. GCs were kept in voltage clamp configuration at -50 mV for at least 1 hr to allow the diffusion of dyes to mf boutons. Recordings were obtained in ACSF solution containing in (mM): 124 NaCl, 2.5 KCl, 26 $NaHCO_3$, 1 NaH_2PO_4, 4 $CaCl_2$, 0 $MgSO_4$, 10 glucose, 0.01 NBQX, 0.1 picrotoxin, and 0.01 D-serine. Using an Ultima 2P laser scanning microscope (Bruker Corp) equipped with an Insight Deep See laser (Spectra Physics) tuned to 830 nm, the "red" photomultiplier tube (PMT) was turned on and with minimal pockel power the red signal was used to identify the mf axon. With 512 x 512 pixel resolution mf axons were followed for at least 200 µm from the DG towards CA3, until bouton structures were morphologically identified and measured (>3 µm in diameter). GCs were switched to current clamp mode held at -70 mV and 1 ms current injections were used to elicit a burst of 5 action potentials at 25 Hz. Using line scan analysis software (PrairieView 5.4, Bruker Corp.), a line was drawn across the diameter of the bouton at a magnification of at least 16X. The “green” PMT channel was turned on and 1,000 line scans were acquired in a 2 s period. Action potential induction was delayed for 400 ms to collect a baseline fluorescence time period. Calcium transients (CaTs) were acquired with a 1 min inter-trial-interval and analyzed using the $\Delta G/R$ calculation: $(G - G_0)/R$. CaTs from control animals were compared to *Grin1*-cKO by taking the mean peak $\Delta G/R$ value for a 30 ms period of the 5th action potential. In similar fashion, CaT signals in acute rat hippocampal slices were acquired and tested for sensitivity to D-APV (100 µM) while adjusting ACSF $MgS0_4$ concentration to 1.3 mM and $CaCl_2$ to 2.5 mM in the absence of NBQX.

For glutamate uncaging experiments, GCs that were mCherry+ were patch-loaded using the internal solution previously described, and a small volume (12 mL) of recirculated ACSF solution containing in (mM): 124 NaCl, 2.5 KCl, 26 $NaHCO_3$, 1 NaH_2PO_4, 4 $CaCl_2$, 0 $MgSO_4$, 10 glucose, 2.5 MNI-glutamate, 0.01 NBQX, 0.1 picrotoxin, and 0.01 D-serine. A MaiTai HP laser (Spectra Physics) was tuned to 720 nm to optimally uncage glutamate and elicit CaTs in GC

dendritic spines. Following the measurement of CaTs in GC spines, mf boutons were identified and to mimic bursting activity, 5 uncaging pulses (1 ms duration) were delivered at 25 Hz. The acquired CaTs in spines and boutons were analyzed using the ΔG/R calculation in control and *Grin1*-cKO animals. In a subset of control boutons, D-APV (100 µM) was applied to detect CaT sensitivity to NMDAR antagonism.

Two-photon BDNF-phluorin imaging

Grin1 floxed and control mice of both sexes (P16-20) were injected with a 1:2 mix of AAV5-CamKII-mCherryCre/AAV-DJ-DIO-BDNF-phluorin viruses targeting the DG using the same coordinates as above. At least four weeks post-surgery acute hippocampal slices were prepared as previously described and slices showing optimal GFP and mCherry expression were taken for imaging sessions. For stimulation, a monopolar micropipette electrode was placed in the *stratum lucidum* at least 250 µm away from the imaging site. The Insight Deep See laser (Spectra Physics) was tuned to 880 nm and the imaging site was selected by the appearance of fibers and bouton structures in the *stratum lucidum*. Using 512 X 512 pixel resolution identified boutons measuring at least 3 µm in diameter were selected as a region of interest (ROI) magnified to 4-6X and a baseline acquisition of 100 consecutive images at 1 Hz using T-series software (PrairieView 5.4, Bruker Corp.) was acquired (Park et al., 2014). Following the baseline acquisition a repetitive stimulation consisting of 125 pulses at 25 Hz was delivered 2x, triggering an acquisition of 200 consecutive images at 1 Hz. The fluorescence intensity of the bouton ROI was measured using ImageJ software to calculate ΔF/F of the BDNF-pHluorin signal. To verify reactivity of the ROI an isosmotic solution of NH_4Cl (50 mM) was added at the end of the imaging session as previously reported (Park et al., 2014). The same experimental and analysis procedure was implemented to measure BDNF release triggered by mf burst stimulation consisting of 5 pulses at 100 Hz, 50x, every 0.5 s.

675 **Viruses**

676 AAV5-CamKII-eGFP and AAV5-CamKII-CreGFP viruses were acquired from UPenn Vector
677 Core. AAV5-CamKII-mCherry and AAV5-CamKII-mCherry-Cre were obtained from UNC Chapel
678 Hill Vector Core. The AAV-DJ-FLEX-ChIEF-tdTomato and AAV-DJ-DIO-BDNF-phluorin viruses
679 were custom ordered and obtained from UNC Chapel Hill Vector Core. The DNA of the ChIEF
680 virus was a generous gift from Dr. Pascal Kaeser (Harvard University), and the DNA of the
681 BDNF-pHluorin was kindly provided by Dr. Hyungju Park (Korea Brain Research Institute).

682

683 **Chemicals & Drugs**

684 Picrotoxin and all chemicals used to prepare cutting, recording, and internal solutions were
685 acquired from MilliporeSigma. All NMDAR antagonists (D-APV, MK-801, R-CPP), NMDAR
686 agonist (D-serine), the group 2/3 mGluR agonist (DCG-IV) and MNI-glutamate for uncaging
687 experiments were purchased from Tocris Bioscience. D-APV was also acquired from the NIMH
688 Chemical Synthesis Drug Program. NBQX was purchased from Cayman Chemical Company.
689 The noncompetitive AMPAR selective antagonist LY303070 was custom ordered from ABX
690 Chemical Company. Alexa 594 morphological dye, Alexa 488, and the Ca^{2+} indicator Fluo-5F
691 (Invitrogen) were purchased from ThermoFisher Scientific.

692

693 **Statistical analysis and Data Acquisition**

694 All data points from experiments were tested for normality using a Shapiro-Wilk test (p value <
695 5% for a normal distribution). Statistical significance was determined if p value < 0.05.
696 Experiments with a normal distribution and an N > to 7 cells were tested for statistical
697 significance with a paired Student *t*-test. Experiments with N < 7 cells or skewed distributions
698 were tested for statistical significance using a paired Wilcoxon signed rank sum test. For
699 experiments comparing control and *Grin1*-cKO animals, statistical significance was determined
700 using Unpaired *t*-test and Mann-Whitney test (U < 0.05). All statistical tests were performed

701 using Origin Pro 9 (Origin Lab). Experimenters were blind to the identity of the virus injected in
702 transgenic *Grin1* floxed mice during the acquisition of data in CA3 electrophysiology and two-
703 photon imaging. However, data analysis could not be performed blind in those experiments in
704 which NMDAR/AMPAR ratios in GCs were examined in order to assess the efficiency of the
705 cKO.
706

707

708 **Figure Legends**

709 **Figure 1. Anatomical and functional evidence for preNMDARs at mossy fiber synapses.**
710 (**A**) Image of a mossy fiber (mf) giant bouton and postsynaptic spines (s). (**B, C**) Higher
711 magnification of mf synapses. Arrows indicate postsynaptic GluN1 whereas arrowheads indicate
712 presynaptic GluN1. Calibration bars: 500 nm. (**D**) Mossy fiber (mf) and associational
713 commissural (ac) synaptic GluN1 immuno-particle radial distribution (30 nm bins), mf: 34
714 synapses, 100 presynaptic particles; ac: 25 synapses, 24 presynaptic particles; 3 animals. (**E**)
715 AMPAR-ESPCs were recorded at V_h= -70 mV in the presence of 0.5 μM LY303070 and 100 μM
716 picrotoxin. Low-frequency facilitation (LFF), induced by stepping stimulation frequency from 0.1
717 to 1 Hz, was assessed before and after bath application of MK-801 (50 μM). MK-801
718 significantly reduced LFF (baseline 378 ± 57%, MK-801 270 ± 48%, n = 10 cells, 9 animals;
719 baseline vs MK-801, p = 3.8 x 10^{-5}, paired *t*-test). In all panels of this figure: representative
720 traces (*top*), representative experiment (*middle*), normalized LFF and summary plot (*bottom*).
721 DCG-IV (1 μM) was applied at the end of all recordings to confirm mf-CA3 transmission. (**F**) D-
722 APV (100 μM) or R-CPP (50 μM) application also reduced LFF (baseline 546 ± 50%, D-APV/R-
723 CPP 380 ± 38%, n = 7 cells, 5 animals; baseline vs D-APV/R-CPP, p = 0.00743, paired *t*-test).
724 (**G**) KAR-EPSCs were recorded at V_h= -70 mV in the presence of 15 μM LY303070 and 100 μM
725 picrotoxin. In addition, NMDAR-mediated transmission was blocked intracellularly by loading
726 MK-801 (2 mM) in the patch-pipette. Bath application of MK-801 (50 μM) significantly reduced
727 LFF (baseline 278 ± 40%, MK-801 195 ± 26% n = 8 cells, 6 animals; baseline vs MK-801, p =
728 0.00259, paired *t*-test). Data are presented as mean ± s.e.m. ** p < 0.01; *** p < 0.005; **** p <
729 0.001.

730

731 **Figure 1-figure supplement 1**. Immunogold-EM reveals negligible presynaptic AMPAR particle
732 distribution. (**A,B**) Images of mossy fiber (mf) and associational commissural (ac) synapses,

733 postsynaptic spines (s). (**C**) AMPAR immuno-particle distribution (30 nm bins), mf: 102
734 synapses, 8 presynaptic particles; ac: 75 synapses, 6 presynaptic particles; 3 animals. Dashed
735 line represents synaptic cleft.
736
737 **Figure 1-figure supplement 2.** (**A**) Stable low-frequency facilitation (LFF) of AMPAR-EPSCs. In
738 naïve slices (interleaved experiments), LFF remained unchanged throughout the recording
739 session (baseline 335 ± 62%, naïve 363 ± 63%, n = 10 cells, 9 animals; p = 0.185, Wilcoxon-
740 Signed Ranks test, baseline vs naÏve). DCG-IV (1 μM) was applied at the end of all recordings
741 to confirm mf-CA3 transmission. (**B**) LFF of KAR-EPSCs was also stable in interleaved, naïve
742 slices (baseline 274 ± 33%, naïve 278 ± 25%, n = 9 cells, 6 animals; p = 0.236, Wilcoxon
743 Signed Ranks test, baseline vs naïve). NBQX (10 μM) was applied at the end of all recordings
744 to confirm mf KAR transmission. Data are presented as mean ± s.e.m.
745
746 **Figure 1-figure supplement 3.** Intracellular MK-801 effectively blocked postsynaptic NMDARs.
747 Representative NMDAR-EPSCs (V_h = + 40 mV) from CA3 pyramidal neurons patch-loaded with
748 2 mM MK-801 *(left)* or naïve internal solution *(right)*. Mf inputs were stimulated with a bipolar
749 electrode (theta-glass pipette) in *stratum lucidum* delivering in the presence of picrotoxin (100
750 μM) and NBQX (10 μM). Bath-application of MK-801 (50 μM) blocked NMDAR currents in naïve
751 cells to a similar magnitude as cells patch-loaded with MK-801 (n = 5 cells, 4 animals in each
752 condition; U = 0.676, Mann-Whitney test). Note that CA3 pyramidal neurons were loaded for at
753 least 3-5 minutes before recording started at +40 mV.
754
755 **Figure 2. GluN1 deletion from granule cells reduces mf-CA3 facilitation.** (**A**)
756 Representative images showing GCs patch-loaded with Alexa 594 (35 μM) *(left),* and GFP
757 expression in GCs *(right)*. (**B**) Representative EPSCs recorded from control (GFP^+) and *Grin1*-
758 cKO (Cre-GFP^+) GCs. Synaptic responses were elicited by activating medial perforant-path

759 inputs. AMPAR-ESPCs were recorded at V_h= -65 mV in the presence of 100 μM picrotoxin,
760 NMDAR-EPSCs were isolated with 10 μM NBQX and recorded at +40 mV. MK-801 (20 μM) was
761 applied at the end of each recording. (**C**) Summary plot demonstrating that GluN1 deletion from
762 GCs virtually abolished NMDAR-mediated transmission indicated by a strong reduction of
763 NMDAR/AMPAR in *Grin1*-cKO GCs as compared to controls (control 1.61 ± 0.18, n = 9 cells, 9
764 animals, *Grin1*-cKO 0.18 ± 0.04, n = 10 cells, 10 animals; control vs *Grin1*-cKO, p = 9.2 x 10^{-6},
765 unpaired *t*-test). (**D**) LFF was significantly reduced in GluN1-deficient animals (control, 430 ±
766 5 %, n = 13 cells, 10 animals; *Grin1*-cKO, 291 ± 6 %, n = 11 cells, 10 animals; p = 0.0239,
767 unpaired *t*-test). Representative traces (*left*) and summary plot (*right*). LFF was induced by
768 stepping stimulation frequency from 0.1 to 1 Hz. DCG-IV (1 μM) was added at the end of each
769 experiment. Data are presented as mean ± s.e.m. * p < 0.05; **** p < 0.001.
770
771 **Figure 3. Reduced facilitation by NMDAR antagonism is independent of the GC**
772 **somatodendritic compartment.** (**A**) KAR-EPSCs were recorded at V_h= -70 mV in the presence
773 of 15 μM LY303070 and 100 μM picrotoxin. In addition, NMDAR-mediated transmission was
774 blocked intracellularly by loading MK-801 (2 mM) in the patch-pipette. LFF of KAR-EPSCs was
775 assessed as in Fig. 1G but with transected mf axons (see Methods). Bath application of MK-801
776 (50 μM) significantly reduced LFF (baseline 213 ± 9%, MK-801 181 ± 10%, n = 8 cells, 7
777 animals; baseline vs MK-801, p = 0.002, paired *t*-test). In all panels of this figure: recording
778 arrangement (*inset*), representative traces (*top*), representative experiment (*middle*), normalized
779 LFF and summary plot (*bottom*). (**B**) Stable LFF in transected, naïve slices (baseline 186 ±
780 10%, naïve 196 ± 5%, n = 8 cells, 7 animals; baseline vs naïve, p = 0.278, paired *t*-test). (**C**)
781 LFF was induced before and during puff application of D-APV (2 mM) in *stratum lucidum*. This
782 manipulation significantly reduced facilitation (baseline 220 ± 19%, D-APV puff 176 ± 11%, n = 7
783 cells, 7 animals; baseline vs D-APV puff, p = 0.003, paired *t*-test). (**D**) Stable LFF in acute slices
784 during puff application of ACSF (baseline 210% ± 12, naïve 213% ± 9, n = 7 cells, 7 animals;

785 baseline vs naïve, p = 0.778, paired *t*-test). NBQX (10 μM) was applied at the end of all
786 recordings to confirm mf KAR transmission. Data are presented as mean ± s.e.m. *** p < 0.005.
787
788 **Figure 3-figure supplement 1.** Targeting preNMDARs located in mf axons but not granule
789 cells. (**A**) Field view of a representative hippocampal slice showing a surgical cut between DG
790 and CA3. (**B**) Local D-APV puff application (vertical arrow, 2 puffs at 0.1 Hz) blocks NMDAR
791 currents recorded at V_h= -50 mV and washes out in less than 10 minutes (n = 7 cells, 5 animals,
792 p = 5 x 10^{-8}, paired *t*-test). Inset depicts the recording paradigm of the experiment *(left)*, the
793 representative NMDAR currents *(top)* and the summary time course *(bottom)* where arrows
794 denote the onset of D-APV (2 mM) puff application. Mfs were stimulated with a bipolar electrode
795 (theta-glass pipette) in *stratum lucidum* in the presence of 100 μM picrotoxin and 10 μM NBQX.
796 (**C**) D-APV puff application in CA3 did not reduce NMDAR transmission in GCs (n = 6 cells, 5
797 animals, control vs D-APV puff, U = 0.594, Mann Whitney test). Excitatory inputs were
798 stimulated with a monopolar electrode placed in the medial molecular layer/inner molecular
799 layer, in the presence of 100 μM picrotoxin and 10 μM NBQX, while GCs were clamped at V_h=
800 +40 mV. Data are presented as mean ± s.e.m.
801
802 **Figure 4. PreNMDARs contribute significantly to burst-induced facilitation and spike**
803 **transfer.** (**A**) Representative images showing expression of GFP-Cre *(left)* and ChIEF-
804 tdTomato *(right)* in the DG of control and *Grin1*-cKO animals. (**B**) Representative AMPAR-
805 EPSCs from control *(left)* and *Grin1*-cKO *(right)* CA3 pyramidal neurons recorded at V_h= -65 mV
806 and evoked by optical burst-stimulation (5 pulses at 25 Hz) of *stratum lucidum*. Blue arrows
807 indicate light stimulation. (**C**) Summary plot of burst-induced facilitation measured as P5/P1
808 ratio of optical responses; facilitation was significantly reduced in *Grin1*-cKO animals as
809 compared to control (*Grin1*-cKO 187 ± 16%, n = 12 cells, 9 animals; control 255 ± 22%, n = 9
810 cells, 8 animals; *Grin1*-cKO vs control, p = 0.0167, unpaired *t*-test). (**D**) Burst-stimulation

811 induced KAR-EPSCs were isolated and recorded as described in Fig. 3, bath-application of MK-
812 801 (50 μM) significantly reduced facilitation (baseline 601 ± 107%, MK-801 464 ± 84%, n = 13
813 cells, 10 animals; baseline vs MK-801, p = 0.00042, paired *t*-test). In panels D and E of this
814 figure: representative traces (*left*), representative experiment (*middle*), and summary plot (*right*).
815 (**E**) Burst-induced facilitation was stable in interleaved, naïve slices (baseline 369 ± 45%, naïve
816 367 ± 48%, n = 9 cells, 9 animals; p = 0.863, paired *t*-test). (**F**) Bath-application of MK-801 (50
817 μM) reduced KAR-mediated action potentials induced by burst-stimulation (baseline 0.93 ± 0.17,
818 MK-801 0.46 ± 0.09, n = 6 cells, 5 animals; p = 0.036, Wilcoxon Signed Ranks test). In panels F
819 and G of this figure: representative traces (*top)*, representative experiment and summary plot
820 (*bottom)*. (**G**) Stable KAR-mediated action potentials in interleaved naïve slices (baseline 0.76 ±
821 0.07, naïve 0.88 ± 0.1, n = 6 cells, 5 animals; p = 0.2084, Wilcoxon Signed Ranks test). NBQX
822 (10 μM) was applied at the end of all experiments in panels D-G. Data are presented as mean
823 ± s.e.m. * p < 0.05; **** p < 0.001.
824
825 **Figure 4-figure supplement 1.** PreNMDARs contribute to burst-induced facilitation in more
826 physiological conditions: 1.2 mM Mg^{+2}, 1.2 mM Ca^{+2} and 35 ºC. KAR-EPSCs were recorded
827 from CA3 pyramidal cells loaded with 2 mM MK-801 in the presence of 15 μM LY303070 and
828 100 μM picrotoxin. (**A**) Bath-application of MK-801 (50 μM) significantly reduced burst-induced
829 facilitation elicited by 5 pulses, 25 Hz (baseline 450 ± 67%, MK-801 366 ± 63%, n = 6 cells, 4
830 animals; baseline vs MK-801, p = 0.036, Wilcoxon Signed Ranks test). In panels A and B of this
831 figure: representative traces (*left*), representative experiment (*middle*), and summary plot (*right*).
832 (**B**) Burst-induced facilitation was stable in interleaved, naïve slices (baseline 462 ± 63%, naïve
833 481 ± 71%, n = 5 cells, 4 animals; p = 0.281, Wilcoxon Signed Ranks test). Data are presented
834 as mean ± s.e.m. * p < 0.05.
835
836 **Figure 4-figure supplement 2.** PreNMDARs contribute to action potential firing elicited by

837 AMPAR-mediated transmission. (**A**) Bath-application of MK-801 (50 μM) reduced action
838 potentials induced by 5 pulses at 25 Hz burst-stimulation (baseline 2.47 ± 0.27, MK-801 1.9 ±
839 0.24, n = 6 cells, 5 animals; p = 0.036, Wilcoxon Signed Ranks test). In panels A and B of this
840 figure: representative traces (*top)*, representative experiment and summary plot (*bottom)*. (**B**)
841 Stable action potential firing in interleaved naïve slices (baseline 1.55 ± 0.24, naïve 1.61 ± 0.23,
842 n = 6 cells, 5 animals; p = 0.402, Wilcoxon Signed Ranks test). DCG-IV (1 μM) was applied at
843 the end of all experiments in panels A-B. Data are presented as mean ± s.e.m. * $p < 0.05$.
844
845 **Figure 4-figure supplement 3.** Intracellular MK-801 effectively blocked postsynaptic NMDARs
846 elicited by burst stimulation (5 pulses at 25 Hz). Representative NMDAR-EPSCs (V_h = + 40 mV)
847 from CA3 pyramidal neurons patch-loaded with 2 mM MK-801 *(left)* or naïve internal solution
848 *(right)*. Mf inputs were stimulated with a bipolar electrode (theta-glass pipette) in *stratum*
849 *lucidum* delivering in the presence of picrotoxin (100 μM) and NBQX (10 μM). NMDAR currents
850 were recorded at V_h= + 40 mV *(gray shaded area)* followed by a voltage jump to -70 mV in iMK-
851 801 conditions and -50 mV in naïve recordings. Bath-application of MK-801 (50 μM) blocked
852 NMDAR currents of the 5th pulse to a similar magnitude as iMK-801 (n = 5 cells, 4 animals per
853 condition; U = 0.21, Mann-Whitney test). Data are presented as mean ± s.e.m.
854
855 **Figure 5. preNMDARs contribute to presynaptic Ca^{2+} rise.** (**A**) Representative images
856 showing GCs patch-loaded with Alexa 488 (35 μM) to confirm expression of mCherry *(bottom)*.
857 Representative AMPAR-EPSCs recorded from control *(top)* or *Grin1*-cKO *(middle)* GCs.
858 Synaptic responses were elicited by activating medial perforant-path inputs. AMPAR-ESPCs
859 were recorded at V_h= -65 mV in the presence of 100 μM picrotoxin, NMDAR-EPSCs were
860 isolated with 10 μM NBQX and recorded at +40 mV. MK-801 (20 μM) was applied at the end of
861 each experiment. Summary plot *(bottom)* demonstrating that GluN1 deletion from GCs virtually
862 abolished NMDAR-mediated transmission indicated by a strong reduction of NMDAR/AMPAR in

863 *Grin1*-cKO granule cells as compared to controls (control 0.90 ± 0.17, n = 7 cells, 6 animals;
864 *Grin1*-cKO 0.13 ± 0.05, n = 6 cells, 6 animals; control vs *Grin1*-cKO, p = 3.81 x 10^{-7}, unpaired *t*-
865 test). (**B**) Representative control and *Grin1*-cKO GCs patch-loaded with Fluo-5F (200 μM) and
866 Alexa 594 (35 μM). Arrows indicate the identification of a mf giant bouton, magnified images in
867 white box. (**C**) Three representative mf boutons *(top)* and line scan analysis of calcium
868 transients (CaTs) elicited by 5 action potentials at 25 Hz *(middle,* Fluo-5F*)* and morphological
869 dye (*bottom*, Alexa 594), in Control and *Grin1*-cKO animals. Dotted line (yellow) indicates line
870 scan location. Red Channel, Alexa 594; Green Channel, Fluo-5F. (**D, E**) Peak analysis of the 5th
871 pulse ΔG/R revealed a significant reduction in Ca^{2+} rise of *Grin1*-cKO animals as compared to
872 Control (control 0.046 ± 0.01, n = 10 boutons, 8 animals; *Grin1*-cKO 0.025 ± 0.004, n = 10
873 boutons, 8 animals; control vs. *Grin1*-cKO, U = 0.017, Mann-Whitney test). Arrows indicate mf
874 activation. Data are presented as mean ± s.e.m. * U < 0.05; **** p < 0.001.
875
876 **Figure 5-figure supplement 1.** NMDAR antagonism reveals a reduction in presynaptic Ca^{+2}
877 rise in the presence of 1.3 mM Mg^{+2} and 2.5 mM Ca^{+2}. (**A, B**) Granule cells were patch-loaded
878 with Fluo-5F (200 μM) and Alexa 594 (35 μM). Line scan analysis of mf giant bouton calcium
879 transients (CaTs) in response to action potential (AP) stimulation (5 APs, 25 Hz). (**C**) Line scan
880 signals following D-APV application or naïve conditions. (**D**) D-APV (100 μM) significantly
881 reduced the 5th peak (P5) of CaTs (baseline 0.155 ± 0.04, D-APV 0.138 ± 0.03, n = 13 boutons,
882 10 animals; baseline vs D-APV, p = 0.00642, Wilcoxon Signed Ranks test). (**E**) In naïve
883 conditions P5 of CaTs is stable (baseline 0.104 ± 0.026, naïve 0.105 ± 0.026, n = 12 boutons,
884 10 animals; baseline vs naïve, p = 0.255, Wilcoxon Signed Ranks test). The first peak (P1) of
885 CaTs is not affected by D-APV (baseline 0.05 ± 0.017; D-APV 0.047 ± 0.014; baseline vs D-
886 APV, p = 0.485, Wilcoxon Signed Ranks test) and is stable in naïve conditions (baseline 0.033 ±
887 0.009; naïve 0.032 ± 0.009, baseline vs naïve, p = 0.196, Wilcoxon Signed Ranks test). Data
888 are presented as mean ± s.e.m. ** p < 0.01.

889

890 **Figure 6. Uncaging glutamate induces Ca^{2+} rise mossy fiber boutons.** (**A**) Representative
891 images showing dendritic spines in GCs *(left)* and mf boutons *(right),* and the associated line
892 scan analysis of calcium transients (CaTs) elicited by uncaging of MNI-glutamate (see
893 Methods), in control and *Grin1*-cKO animals. Blue dots indicate uncaging spots. Red Channel,
894 Alexa 594; Green Channel, Fluo-5F. (**B**) Line scan analysis of CaTs measuring ΔG/R in
895 dendritic spines when MNI-glutamate is uncaged in control or *Grin1*-cKO animals. Blue dots
896 indicate location of two photon uncaging (2PU) pulses. (**C**) Summary plot demonstrating a
897 significant reduction in dendritic spine CaTs in *Grin1*-cKO as compared to Control (control 0.053
898 ± 0.01 ΔG/R, n = 6 dendritic spines, 6 animals; *Grin1*-cKO 0.004 ± 0.003 ΔG/R, n = 6 spines, 6
899 animals; ΔG/R control vs. *Grin1*-cKO, p = 0.00088, unpaired *t*-test). (**D**) Line scan analysis of
900 CaTs measuring ΔG/R in mf boutons when MNI-glutamate is uncaged in control or *Grin1*-cKO
901 animals. (**E**) Summary plot demonstrating significant CaTs in boutons of control as compared to
902 *Grin1*-cKO (control 0.014 ± 0.005, n = 6 boutons, 6 animals; *Grin1*-cKO -0.00012 ± -0.0006, n =
903 6 boutons, 6 animals; control vs. *Grin1*-cKO, p = 0.015, unpaired *t*-test). Data are presented as
904 mean ± s.e.m. * $p < 0.05$; **** $p < 0.001$.

905

906 **Figure 6-figure supplement 1.** *Grin1*-cKO exhibit reduced CaTs at varying uncaging laser
907 power intensities. (**A**) Representative images of CaTs from control *(top)* and G*rin1*-cKO animals
908 *(bottom)* after MNI-glutamate uncaging (2 mM, 3 pulses at 25 Hz) on GC dendritic spines.
909 Dotted line (yellow) indicates line scan, and blue dots indicate 2PU spots. (**B**) Quantified ΔG/R
910 signals *(top)* and uncaging induced NMDAR-EPSCs *(bottom)* from control and *Grin1*-cKO
911 animals. Blue dots indicate when 2PU pulses were delivered. (**C**) Control animals display robust
912 ΔG/R signals as compared to *Grin1*-cKO animals at varying laser power intensities (6 spines, 6
913 animals per group, U = 0.00507 per power intensity, Mann-Whitney test). Data are presented as
914 mean ± s.e.m. ** $U < 0.01$.

915

916 **Figure 6-figure supplement 2.** Bouton CaTs can be detected after repetitive uncaging of MNI-
917 glutamate. (**A**) Representative images of CaTs from single-trial: 1 pulse *(top)* and 5 pulses, 25
918 Hz *(bottom)* of MNI-glutamate uncaging (2 mM). Dotted line (yellow) indicates line scan, and
919 blue dots indicate 2PU spots. (**B**) Quantified ΔG/R signals from 1 pulse *(black)* and 5 pulses
920 *(dark gray)* from all trials. (**C**) Repetitive pulses result in larger ΔG/R signals as compared to
921 single pulses (n = 6 boutons, 6 animals, p = 0.03603, Wilcoxon-Signed Ranks test). Data are
922 presented as mean ± s.e.m. * p < 0.05.

923

924 **Figure 6-figure supplement 3.** NMDAR antagonism with D-APV blocks CaTs elicited by
925 glutamate 2PU. (**A**) Representative image of baseline glutamate uncaging driven CaTs in mf
926 boutons *(top)*. D-APV application (100 μM) blocks CaTs *(bottom)*. (**B**) Quantified ΔG/R signals
927 before and after D-APV application. (**C**) Summary data of D-APV block on glutamate uncaging
928 elicited CaTs (baseline 0.0103 ± 0.0016, D-APV -0.004 ± 0.0024, n = 4 boutons, 3 animals; U =
929 0.0304, Mann-Whitney test, baseline vs D-APV). Data are presented as mean ± s.e.m. * U <
930 0.05.

931

932 **Figure 7. preNMDARs contribute significantly to BDNF release following repetitive**
933 **activity.** (**A**) Representative images showing expression of BDNF-pHluorin in the DG and CA3
934 area (arrows indicate mf axon, arrowheads indicate mf boutons). Control images *(top)*, *Grin1*-
935 cKO images *(bottom)*. (**B**) Representative images of BDNF-pHluorin signal intensity at baseline
936 and after repetitive stimulation of mfs (125 pulses, 25 Hz, x 2). Control images *(left)*, *Grin1*-cKO
937 images *(right*), arrowhead indicates region of interest. (**C**) Time course of BDNF-pHluorin signal
938 intensity measured as ΔF/F (%): control *(black)*, *Grin1*-cKO *(red),* Naïve *(blue)*. (**D**)
939 Quantification of BDNF-pHluorin signal in (C) during the last 100 seconds reveals larger BDNF
940 release in control animals as compared to *Grin1*-cKO (control -18% ± 3%, n = 9 slices, 5

941 animals; *Grin1*-cKO -8 ± 1%, n = 10 slices, 5 animals; *Grin1*-cKO vs. control, p = 0.00648,
942 unpaired *t*-test). Data are presented as mean ± s.e.m. ** p < 0.01.
943
944 **Figure 7-figure supplement 1.** preNMDARs contribute significantly to BDNF release following
945 a more physiological pattern of burst-stimulation. (**A**) Representative images of BDNF-pHluorin
946 signal intensity at baseline and after burst stimulation of mfs (5 pulses, 100 Hz, x 50, every 0.5
947 s). Control images *(left)*, *Grin1*-cKO images *(right*), arrowhead indicates region of interest. (**B**)
948 Time course of BDNF-pHluorin signal intensity measured as ΔF/F (%): control *(black)*, *Grin1*-
949 cKO *(red),* Naïve *(blue)*. (**C**) Quantification of BDNF-pHluorin signal in (B) during the last 100
950 seconds reveals larger BDNF release in control animals as compared to *Grin1*-cKO (control -
951 8.9% ± 2%, n = 7 slices, 5 animals; *Grin1*-cKO -3.5 ± 1%, n = 11 slices, 5 animals; *Grin1*-cKO
952 vs. control, p = 0.0305, unpaired *t*-test). Data are presented as mean ± s.e.m. * p < 0.05.
953
954 **Figure 8. preNMDARs contribute to synaptic facilitation of mossy fiber inputs onto**
955 **mossy cells but not onto CA3 inhibitory interneurons.** (**A**) Representative images showing a
956 CA3 interneuron and a hilar mossy cell patch-loaded with Alexa 594 (35 μM) for morphological
957 identification in acute rat hippocampal slices. (**B**) AMPAR-EPSCs were recorded from CA3
958 interneurons at V_h= -65 mV and burst-stimulation was elicited by 5 pulses at 25 Hz, see traces
959 *(top)*. Representative experiment *(bottom, left)*, and summary plots *(right)* showing bath-
960 application of MK-801 (50 μM) had no significant effect on depression *(top, right)* or facilitation
961 *(bottom, right)* measured by P5/P1 ratio (baseline 54 ± 12%, MK-801 60 ± 16%, n = 6 cells; MK-
962 801 vs baseline, p = 0.675, Wilcoxon Signed Ranks test; baseline 281 ± 30%, MK-801 318 ±
963 37%, n = 7 cells; MK-801 vs baseline, p = 0.178, paired *t*-test, 5 animals in each data set). (**C**)
964 AMPAR-ESPCs were recorded at V_h = -70 mV from hilar mossy cells, LFF was induced by
965 stepping stimulation frequency from 0.1 to 1 Hz, see traces *(top)*. Representative experiment
966 *(middle)*, normalized LFF and summary plot *(bottom)* indicating bath-application of MK-801 (50

967 μM) reduced facilitation (baseline 339 ± 41%, MK-801 258 ± 29%, n = 10 cells, 6 animals;
968 baseline vs MK-801, p = 0.00152, paired *t*-test). DCG-IV (1 μM) was applied at the end of all
969 experiments. Data are presented as mean ± s.e.m. *** p < 0.005.
970
971 **Figure 8-figure supplement 1.** Stability experiments for mf-Interneuron and mf-mossy cell
972 short-term plasticity. (**A**) Stable CA3 interneuron burst-induced facilitation of mf-CA3
973 transmission (baseline 273 ± 30%, naïve 294 ± 33%, n = 10 cells, 6 animals; p = 0.298, paired *t*-
974 test, baseline vs naïve). (**B**) Stable low-frequency facilitation (LFF) of AMPAR-EPSCs in hilar
975 mossy cells (baseline 288 ± 51%, naïve 291 ± 29%, n = 7 cells, 6 animals; p = 0.937, paired *t*-
976 test, baseline vs naïve). DCG-IV (1 μM) was applied at the end of all recordings to confirm mf-
977 CA3 transmission. Data are presented as mean ± s.e.m.
978
979
980
981
982
983
984
985
986
987
988
989
990
991
992

REFERENCES

Abbott, L. F., & Regehr, W. G. (2004). Synaptic computation. *Nature, 431*(7010), 796-803. doi:10.1038/nature03010

Abrahamsson, T., Chou, C. Y. C., Li, S. Y., Mancino, A., Costa, R. P., Brock, J. A., . . . Sjostrom, P. J. (2017). Differential Regulation of Evoked and Spontaneous Release by Presynaptic NMDA Receptors. *Neuron, 96*(4), 839-855 e835. doi:10.1016/j.neuron.2017.09.030

Alle, H., & Geiger, J. R. (2006). Combined analog and action potential coding in hippocampal mossy fibers. *Science, 311*(5765), 1290-1293. doi:10.1126/science.1119055

Amaral, D. G., & Dent, J. A. (1981). Development of the mossy fibers of the dentate gyrus: I. A light and electron microscopic study of the mossy fibers and their expansions. *J Comp Neurol, 195*(1), 51-86. doi:10.1002/cne.901950106

Amaral, D. G., Scharfman, H. E., & Lavenex, P. (2007). The dentate gyrus: fundamental neuroanatomical organization (dentate gyrus for dummies). *Prog Brain Res, 163*, 3-22. doi:S0079-6123(07)63001-5 [pii]
10.1016/S0079-6123(07)63001-5

Banerjee, A., Larsen, R. S., Philpot, B. D., & Paulsen, O. (2016). Roles of Presynaptic NMDA Receptors in Neurotransmission and Plasticity. *Trends Neurosci, 39*(1), 26-39. doi:10.1016/j.tins.2015.11.001

Berg, L. K., Larsson, M., Morland, C., & Gundersen, V. (2013). Pre- and postsynaptic localization of NMDA receptor subunits at hippocampal mossy fibre synapses. *Neuroscience, 230*, 139-150. doi:10.1016/j.neuroscience.2012.10.061

Berretta, N., & Jones, R. S. (1996). Tonic facilitation of glutamate release by presynaptic N-methyl-D-aspartate autoreceptors in the entorhinal cortex. *Neuroscience, 75*(2), 339-344. doi:10.1016/0306-4522(96)00301-6

Bischofberger, J., Engel, D., Frotscher, M., & Jonas, P. (2006). Timing and efficacy of transmitter release at mossy fiber synapses in the hippocampal network. *Pflugers Arch, 453*(3), 361-372. doi:10.1007/s00424-006-0093-2

Bouvier, G., Bidoret, C., Casado, M., & Paoletti, P. (2015). Presynaptic NMDA receptors: Roles and rules. *Neuroscience, 311*, 322-340. doi:10.1016/j.neuroscience.2015.10.033

Bouvier, G., Higgins, D., Spolidoro, M., Carrel, D., Mathieu, B., Lena, C., . . . Casado, M. (2016). Burst-Dependent Bidirectional Plasticity in the Cerebellum Is Driven by Presynaptic NMDA Receptors. *Cell Rep, 15*(1), 104-116. doi:10.1016/j.celrep.2016.03.004

Bouvier, G., Larsen, R. S., Rodriguez-Moreno, A., Paulsen, O., & Sjostrom, P. J. (2018). Towards resolving the presynaptic NMDA receptor debate. *Curr Opin Neurobiol, 51*, 1-7. doi:10.1016/j.conb.2017.12.020

Buchanan, K. A., Blackman, A. V., Moreau, A. W., Elgar, D., Costa, R. P., Lalanne, T., . . . Sjostrom, P. J. (2012). Target-specific expression of presynaptic NMDA receptors in neocortical microcircuits. *Neuron, 75*(3), 451-466. doi:10.1016/j.neuron.2012.06.017

Burke, K. J., Jr., & Bender, K. J. (2019). Modulation of Ion Channels in the Axon: Mechanisms and Function. *Front Cell Neurosci, 13*, 221. doi:10.3389/fncel.2019.00221

Carter, B. C., & Jahr, C. E. (2016). Postsynaptic, not presynaptic NMDA receptors are required for spike-timing-dependent LTD induction. *Nat Neurosci, 19*(9), 1218-1224. doi:10.1038/nn.4343

Castillo, P. E. (2012). Presynaptic LTP and LTD of excitatory and inhibitory synapses. *Cold Spring Harb Perspect Biol, 4*(2). doi:10.1101/cshperspect.a005728

Castillo, P. E., Malenka, R. C., & Nicoll, R. A. (1997). Kainate receptors mediate a slow postsynaptic current in hippocampal CA3 neurons. *Nature, 388*(6638), 182-186. doi:10.1038/40645

Chamberland, S., Timofeeva, Y., Evstratova, A., Volynski, K., & Toth, K. (2018). Action potential counting at giant mossy fiber terminals gates information transfer in the hippocampus.

Proc Natl Acad Sci U S A, 115(28), 7434-7439. doi:10.1073/pnas.1720659115

Chen, W., Walwyn, W., Ennes, H. S., Kim, H., McRoberts, J. A., & Marvizon, J. C. (2014). BDNF released during neuropathic pain potentiates NMDA receptors in primary afferent terminals. *Eur J Neurosci, 39*(9), 1439-1454. doi:10.1111/ejn.12516

Chen, Y., Chen, S. R., Chen, H., Zhang, J., & Pan, H. L. (2019). Increased alpha2delta-1-NMDA receptor coupling potentiates glutamatergic input to spinal dorsal horn neurons in chemotherapy-induced neuropathic pain. *J Neurochem, 148*(2), 252-274. doi:10.1111/jnc.14627

Christie, J. M., & Jahr, C. E. (2008). Dendritic NMDA receptors activate axonal calcium channels. *Neuron, 60*(2), 298-307. doi:10.1016/j.neuron.2008.08.028

Christie, J. M., & Jahr, C. E. (2009). Selective expression of ligand-gated ion channels in L5 pyramidal cell axons. *J Neurosci, 29*(37), 11441-11450. doi:10.1523/JNEUROSCI.2387-09.2009

Conner, J. M., Lauterborn, J. C., Yan, Q., Gall, C. M., & Varon, S. (1997). Distribution of brain-derived neurotrophic factor (BDNF) protein and mRNA in the normal adult rat CNS: evidence for anterograde axonal transport. *J Neurosci, 17*(7), 2295-2313. Retrieved from https://www.ncbi.nlm.nih.gov/pubmed/9065491

Corlew, R., Brasier, D. J., Feldman, D. E., & Philpot, B. D. (2008). Presynaptic NMDA receptors: newly appreciated roles in cortical synaptic function and plasticity. *Neuroscientist, 14*(6), 609-625. doi:10.1177/1073858408322675

Corlew, R., Wang, Y., Ghermazien, H., Erisir, A., & Philpot, B. D. (2007). Developmental switch in the contribution of presynaptic and postsynaptic NMDA receptors to long-term depression. *J Neurosci, 27*(37), 9835-9845. doi:10.1523/JNEUROSCI.5494-06.2007

Cull-Candy, S., Brickley, S., & Farrant, M. (2001). NMDA receptor subunits: diversity, development and disease. *Curr Opin Neurobiol, 11*(3), 327-335. Retrieved from https://www.ncbi.nlm.nih.gov/pubmed/11399431

Diamantaki, M., Frey, M., Berens, P., Preston-Ferrer, P., & Burgalossi, A. (2016). Sparse activity of identified dentate granule cells during spatial exploration. *Elife, 5*. doi:10.7554/eLife.20252

Dore, K., Aow, J., & Malinow, R. (2016). The Emergence of NMDA Receptor Metabotropic Function: Insights from Imaging. *Front Synaptic Neurosci, 8*, 20. doi:10.3389/fnsyn.2016.00020

Duguid, I. C. (2013). Presynaptic NMDA receptors: are they dendritic receptors in disguise? *Brain Res Bull, 93*, 4-9. doi:10.1016/j.brainresbull.2012.12.004

Duguid, I. C., & Smart, T. G. (2009). Presynaptic NMDA Receptors. In A. M. Van Dongen (Ed.), *Biology of the NMDA Receptor*. Boca Raton (FL).

Engelman, H. S., & MacDermott, A. B. (2004). Presynaptic ionotropic receptors and control of transmitter release. *Nat Rev Neurosci, 5*(2), 135-145. doi:10.1038/nrn1297

Evstratova, A., & Toth, K. (2014). Information processing and synaptic plasticity at hippocampal mossy fiber terminals. *Front Cell Neurosci, 8*, 28. doi:10.3389/fncel.2014.00028

Fujisawa, S., & Aoki, C. (2003). In vivo blockade of N-methyl-D-aspartate receptors induces rapid trafficking of NR2B subunits away from synapses and out of spines and terminals in adult cortex. *Neuroscience, 121*(1), 51-63. doi:10.1016/s0306-4522(03)00341-5

Gill, I., Droubi, S., Giovedi, S., Fedder, K. N., Bury, L. A., Bosco, F., . . . Sabo, S. L. (2015). Presynaptic NMDA receptors - dynamics and distribution in developing axons in vitro and in vivo. *J Cell Sci, 128*(4), 768-780. doi:10.1242/jcs.162362

GoodSmith, D., Chen, X., Wang, C., Kim, S. H., Song, H., Burgalossi, A., . . . Knierim, J. J. (2017). Spatial Representations of Granule Cells and Mossy Cells of the Dentate Gyrus. *Neuron, 93*(3), 677-690 e675. doi:10.1016/j.neuron.2016.12.026

Hagena, H., & Manahan-Vaughan, D. (2010). Frequency facilitation at mossy fiber-CA3 synapses of freely behaving rats contributes to the induction of persistent LTD via an

adenosine-A1 receptor-regulated mechanism. *Cereb Cortex, 20*(5), 1121-1130. doi:10.1093/cercor/bhp184

Henze, D. A., Urban, N. N., & Barrionuevo, G. (2000). The multifarious hippocampal mossy fiber pathway: a review. *Neuroscience, 98*(3), 407-427. Retrieved from https://www.ncbi.nlm.nih.gov/pubmed/10869836

Henze, D. A., Wittner, L., & Buzsaki, G. (2002). Single granule cells reliably discharge targets in the hippocampal CA3 network in vivo. *Nat Neurosci, 5*(8), 790-795. doi:10.1038/nn887

Jackman, S. L., & Regehr, W. G. (2017). The Mechanisms and Functions of Synaptic Facilitation. *Neuron, 94*(3), 447-464. doi:10.1016/j.neuron.2017.02.047

Jourdain, P., Bergersen, L. H., Bhaukaurally, K., Bezzi, P., Santello, M., Domercq, M., . . . Volterra, A. (2007). Glutamate exocytosis from astrocytes controls synaptic strength. *Nat Neurosci, 10*(3), 331-339. doi:10.1038/nn1849

Kamiya, H., Shinozaki, H., & Yamamoto, C. (1996). Activation of metabotropic glutamate receptor type 2/3 suppresses transmission at rat hippocampal mossy fibre synapses. *J Physiol, 493 (Pt 2)*, 447-455. doi:10.1113/jphysiol.1996.sp021395

Klug, A., Borst, J. G., Carlson, B. A., Kopp-Scheinpflug, C., Klyachko, V. A., & Xu-Friedman, M. A. (2012). How do short-term changes at synapses fine-tune information processing? *J Neurosci, 32*(41), 14058-14063. doi:10.1523/JNEUROSCI.3348-12.2012

Kunz, P. A., Roberts, A. C., & Philpot, B. D. (2013). Presynaptic NMDA receptor mechanisms for enhancing spontaneous neurotransmitter release. *J Neurosci, 33*(18), 7762-7769. doi:10.1523/JNEUROSCI.2482-12.2013

Kwon, H. B., & Castillo, P. E. (2008). Role of glutamate autoreceptors at hippocampal mossy fiber synapses. *Neuron, 60*(6), 1082-1094. doi:10.1016/j.neuron.2008.10.045

Larsen, R. S., Corlew, R. J., Henson, M. A., Roberts, A. C., Mishina, M., Watanabe, M., . . . Philpot, B. D. (2011). NR3A-containing NMDARs promote neurotransmitter release and spike timing-dependent plasticity. *Nat Neurosci, 14*(3), 338-344. doi:10.1038/nn.2750

Larsen, R. S., & Sjostrom, P. J. (2015). Synapse-type-specific plasticity in local circuits. *Curr Opin Neurobiol, 35*, 127-135. doi:10.1016/j.conb.2015.08.001

Larsen, R. S., Smith, I. T., Miriyala, J., Han, J. E., Corlew, R. J., Smith, S. L., & Philpot, B. D. (2014). Synapse-specific control of experience-dependent plasticity by presynaptic NMDA receptors. *Neuron, 83*(4), 879-893. doi:10.1016/j.neuron.2014.07.039

Lau, C. G., & Zukin, R. S. (2007). NMDA receptor trafficking in synaptic plasticity and neuropsychiatric disorders. *Nat Rev Neurosci, 8*(6), 413-426. doi:10.1038/nrn2153

Lawrence, J. J., & McBain, C. J. (2003). Interneuron diversity series: containing the detonation--feedforward inhibition in the CA3 hippocampus. *Trends Neurosci, 26*(11), 631-640. doi:10.1016/j.tins.2003.09.007

Liang, Y., Yuan, L. L., Johnston, D., & Gray, R. (2002). Calcium signaling at single mossy fiber presynaptic terminals in the rat hippocampus. *J Neurophysiol, 87*(2), 1132-1137. doi:10.1152/jn.00661.2001

Lujan, R., Nusser, Z., Roberts, J. D., Shigemoto, R., & Somogyi, P. (1996). Perisynaptic location of metabotropic glutamate receptors mGluR1 and mGluR5 on dendrites and dendritic spines in the rat hippocampus. *Eur J Neurosci, 8*(7), 1488-1500. Retrieved from https://www.ncbi.nlm.nih.gov/pubmed/8758956

Lysetskiy, M., Foldy, C., & Soltesz, I. (2005). Long- and short-term plasticity at mossy fiber synapses on mossy cells in the rat dentate gyrus. *Hippocampus, 15*(6), 691-696. doi:10.1002/hipo.20096

Madara, J. C., & Levine, E. S. (2008). Presynaptic and postsynaptic NMDA receptors mediate distinct effects of brain-derived neurotrophic factor on synaptic transmission. *J Neurophysiol, 100*(6), 3175-3184. doi:10.1152/jn.90880.2008

Mameli, M., Carta, M., Partridge, L. D., & Valenzuela, C. F. (2005). Neurosteroid-induced plasticity of immature synapses via retrograde modulation of presynaptic NMDA

1148 receptors. *J Neurosci, 25*(9), 2285-2294. doi:10.1523/JNEUROSCI.3877-04.2005
1149 Martin, D., Bustos, G. A., Bowe, M. A., Bray, S. D., & Nadler, J. V. (1991). Autoreceptor
1150 regulation of glutamate and aspartate release from slices of the hippocampal CA1 area.
1151 *J Neurochem, 56*(5), 1647-1655. doi:10.1111/j.1471-4159.1991.tb02063.x
1152 McGuinness, L., Taylor, C., Taylor, R. D., Yau, C., Langenhan, T., Hart, M. L., . . . Emptage, N. J.
1153 (2010). Presynaptic NMDARs in the hippocampus facilitate transmitter release at theta
1154 frequency. *Neuron, 68*(6), 1109-1127. doi:10.1016/j.neuron.2010.11.023
1155 McHugh, T. J., Jones, M. W., Quinn, J. J., Balthasar, N., Coppari, R., Elmquist, J. K., . . .
1156 Tonegawa, S. (2007). Dentate gyrus NMDA receptors mediate rapid pattern separation
1157 in the hippocampal network. *Science, 317*(5834), 94-99. doi:10.1126/science.1140263
1158 McNamara, J. O., & Scharfman, H. E. (2012). Temporal Lobe Epilepsy and the BDNF Receptor,
1159 TrkB. In th, J. L. Noebels, M. Avoli, M. A. Rogawski, R. W. Olsen, & A. V. Delgado-
1160 Escueta (Eds.), *Jasper's Basic Mechanisms of the Epilepsies*. Bethesda (MD).
1161 Miller, R. J. (1998). Presynaptic receptors. *Annu Rev Pharmacol Toxicol, 38*, 201-227.
1162 doi:10.1146/annurev.pharmtox.38.1.201
1163 Nicoll, R. A., & Schmitz, D. (2005). Synaptic plasticity at hippocampal mossy fibre synapses. *Nat*
1164 *Rev Neurosci, 6*(11), 863-876. doi:10.1038/nrn1786
1165 Nusser, Z., Lujan, R., Laube, G., Roberts, J. D., Molnar, E., & Somogyi, P. (1998). Cell type and
1166 pathway dependence of synaptic AMPA receptor number and variability in the
1167 hippocampus. *Neuron, 21*(3), 545-559. Retrieved from
1168 https://www.ncbi.nlm.nih.gov/pubmed/9768841
1169 Paoletti, P., Bellone, C., & Zhou, Q. (2013). NMDA receptor subunit diversity: impact on receptor
1170 properties, synaptic plasticity and disease. *Nat Rev Neurosci, 14*(6), 383-400.
1171 doi:10.1038/nrn3504
1172 Park, H., Popescu, A., & Poo, M. M. (2014). Essential role of presynaptic NMDA receptors in
1173 activity-dependent BDNF secretion and corticostriatal LTP. *Neuron, 84*(5), 1009-1022.
1174 doi:10.1016/j.neuron.2014.10.045
1175 Pernia-Andrade, A. J., & Jonas, P. (2014). Theta-gamma-modulated synaptic currents in
1176 hippocampal granule cells in vivo define a mechanism for network oscillations. *Neuron,*
1177 *81*(1), 140-152. doi:10.1016/j.neuron.2013.09.046
1178 Petralia, R. S., Yokotani, N., & Wenthold, R. J. (1994). Light and electron microscope
1179 distribution of the NMDA receptor subunit NMDAR1 in the rat nervous system using a
1180 selective anti-peptide antibody. *J Neurosci, 14*(2), 667-696. Retrieved from
1181 https://www.ncbi.nlm.nih.gov/pubmed/8301357
1182 Pickel, V. M., Colago, E. E., Mania, I., Molosh, A. I., & Rainnie, D. G. (2006). Dopamine D1
1183 receptors co-distribute with N-methyl-D-aspartic acid type-1 subunits and modulate
1184 synaptically-evoked N-methyl-D-aspartic acid currents in rat basolateral amygdala.
1185 *Neuroscience, 142*(3), 671-690. doi:10.1016/j.neuroscience.2006.06.059
1186 Pinheiro, P. S., & Mulle, C. (2008). Presynaptic glutamate receptors: physiological functions and
1187 mechanisms of action. *Nat Rev Neurosci, 9*(6), 423-436. doi:10.1038/nrn2379
1188 Rebola, N., Carta, M., & Mulle, C. (2017). Operation and plasticity of hippocampal CA3 circuits:
1189 implications for memory encoding. *Nat Rev Neurosci, 18*(4), 208-220.
1190 doi:10.1038/nrn.2017.10
1191 Rogers, M., & Dani, J. A. (1995). Comparison of quantitative calcium flux through NMDA, ATP,
1192 and ACh receptor channels. *Biophys J, 68*(2), 501-506. doi:10.1016/S0006-
1193 3495(95)80211-0
1194 Rossi, B., Ogden, D., Llano, I., Tan, Y. P., Marty, A., & Collin, T. (2012). Current and calcium
1195 responses to local activation of axonal NMDA receptors in developing cerebellar
1196 molecular layer interneurons. *PLoS One, 7*(6), e39983.
1197 doi:10.1371/journal.pone.0039983
1198 Salin, P. A., Scanziani, M., Malenka, R. C., & Nicoll, R. A. (1996). Distinct short-term plasticity at

two excitatory synapses in the hippocampus. *Proc Natl Acad Sci U S A, 93*(23), 13304-13309. Retrieved from https://www.ncbi.nlm.nih.gov/pubmed/8917586

Sanz-Clemente, A., Nicoll, R. A., & Roche, K. W. (2013). Diversity in NMDA receptor composition: many regulators, many consequences. *Neuroscientist, 19*(1), 62-75. doi:10.1177/1073858411435129

Savtchouk, I., Di Castro, M. A., Ali, R., Stubbe, H., Lujan, R., & Volterra, A. (2019). Circuit-specific control of the medial entorhinal inputs to the dentate gyrus by atypical presynaptic NMDARs activated by astrocytes. *Proc Natl Acad Sci U S A, 116*(27), 13602-13610. doi:10.1073/pnas.1816013116

Schicker, K. W., Dorostkar, M. M., & Boehm, S. (2008). Modulation of transmitter release via presynaptic ligand-gated ion channels. *Curr Mol Pharmacol, 1*(2), 106-129. doi:10.2174/1874467210801020106

Schildt, S., Endres, T., Lessmann, V., & Edelmann, E. (2013). Acute and chronic interference with BDNF/TrkB-signaling impair LTP selectively at mossy fiber synapses in the CA3 region of mouse hippocampus. *Neuropharmacology, 71*, 247-254. doi:10.1016/j.neuropharm.2013.03.041

Senzai, Y., & Buzsaki, G. (2017). Physiological Properties and Behavioral Correlates of Hippocampal Granule Cells and Mossy Cells. *Neuron, 93*(3), 691-704 e695. doi:10.1016/j.neuron.2016.12.011

Siegel, S. J., Brose, N., Janssen, W. G., Gasic, G. P., Jahn, R., Heinemann, S. F., & Morrison, J. H. (1994). Regional, cellular, and ultrastructural distribution of N-methyl-D-aspartate receptor subunit 1 in monkey hippocampus. *Proc Natl Acad Sci U S A, 91*(2), 564-568. Retrieved from https://www.ncbi.nlm.nih.gov/pubmed/8290563

Takumi, Y., Ramirez-Leon, V., Laake, P., Rinvik, E., & Ottersen, O. P. (1999). Different modes of expression of AMPA and NMDA receptors in hippocampal synapses. *Nat Neurosci, 2*(7), 618-624. doi:10.1038/10172

Toni, N., & Schinder, A. F. (2015). Maturation and Functional Integration of New Granule Cells into the Adult Hippocampus. *Cold Spring Harb Perspect Biol, 8*(1), a018903. doi:10.1101/cshperspect.a018903

Toth, K., Suares, G., Lawrence, J. J., Philips-Tansey, E., & McBain, C. J. (2000). Differential mechanisms of transmission at three types of mossy fiber synapse. *J Neurosci, 20*(22), 8279-8289. Retrieved from https://www.ncbi.nlm.nih.gov/pubmed/11069934

Traynelis, S. F., Wollmuth, L. P., McBain, C. J., Menniti, F. S., Vance, K. M., Ogden, K. K., . . . Dingledine, R. (2010). Glutamate receptor ion channels: structure, regulation, and function. *Pharmacol Rev, 62*(3), 405-496. doi:10.1124/pr.109.002451

Vandael, D., Borges-Merjane, C., Zhang, X., & Jonas, P. (2020). Short-Term Plasticity at Hippocampal Mossy Fiber Synapses Is Induced by Natural Activity Patterns and Associated with Vesicle Pool Engram Formation. *Neuron, 107*(3), 509-521 e507. doi:10.1016/j.neuron.2020.05.013

Vyleta, N. P., Borges-Merjane, C., & Jonas, P. (2016). Plasticity-dependent, full detonation at hippocampal mossy fiber-CA3 pyramidal neuron synapses. *Elife, 5*. doi:10.7554/eLife.17977

Wang, P. Y., Petralia, R. S., Wang, Y. X., Wenthold, R. J., & Brenowitz, S. D. (2011). Functional NMDA receptors at axonal growth cones of young hippocampal neurons. *J Neurosci, 31*(25), 9289-9297. doi:10.1523/JNEUROSCI.5639-10.2011

Watanabe, M., Fukaya, M., Sakimura, K., Manabe, T., Mishina, M., & Inoue, Y. (1998). Selective scarcity of NMDA receptor channel subunits in the stratum lucidum (mossy fibre-recipient layer) of the mouse hippocampal CA3 subfield. *Eur J Neurosci, 10*(2), 478-487. Retrieved from https://www.ncbi.nlm.nih.gov/pubmed/9749710

Wong, H. H., Rannio, S., Jones, V., Thomazeau, A., & Sjostrom, P. J. (2020). NMDA receptors in axons: there's no coincidence. *J Physiol*. doi:10.1113/JP280059

Woodhall, G., Evans, D. I., Cunningham, M. O., & Jones, R. S. (2001). NR2B-containing NMDA autoreceptors at synapses on entorhinal cortical neurons. *J Neurophysiol, 86*(4), 1644-1651. doi:10.1152/jn.2001.86.4.1644

Yan, Q., Rosenfeld, R. D., Matheson, C. R., Hawkins, N., Lopez, O. T., Bennett, L., & Welcher, A. A. (1997). Expression of brain-derived neurotrophic factor protein in the adult rat central nervous system. *Neuroscience, 78*(2), 431-448. Retrieved from https://www.ncbi.nlm.nih.gov/pubmed/9145800

Yang, J., Woodhall, G. L., & Jones, R. S. (2006). Tonic facilitation of glutamate release by presynaptic NR2B-containing NMDA receptors is increased in the entorhinal cortex of chronically epileptic rats. *J Neurosci, 26*(2), 406-410. doi:10.1523/JNEUROSCI.4413-05.2006

Zeng, J., Thomson, L. M., Aicher, S. A., & Terman, G. W. (2006). Primary afferent NMDA receptors increase dorsal horn excitation and mediate opiate tolerance in neonatal rats. *J Neurosci, 26*(46), 12033-12042. doi:10.1523/JNEUROSCI.2530-06.2006

Zucca, S., Griguoli, M., Malezieux, M., Grosjean, N., Carta, M., & Mulle, C. (2017). Control of Spike Transfer at Hippocampal Mossy Fiber Synapses In Vivo by GABAA and GABAB Receptor-Mediated Inhibition. *J Neurosci, 37*(3), 587-598. doi:10.1523/JNEUROSCI.2057-16.2016

Key Resources Table				
Reagent type (species) or resource	**Designation**	**Source or reference**	**Identifiers**	**Additional information**
strain, strain background (*rattus norvegicus* male and female)	Rat: Sprague-Dawley	Charles River	Strain code: 400	
strain, strain background (*Mus musculus*, male and female)	Mouse: *Grin1*$^{fl/fl}$ (B6.129S4-*Grin1*^{tm2Stl}/J)	Dr. Michael Higley /The Jackson Laboratory	RRID: IMSR_JAX: 005246	
strain, strain background (*Mus musculus* male and female)	Mouse: C57Bl6/J	Charles River	Strain code: 027	
antibody	(Include host species and clonality) Mouse, Monoclonal, anti-NMDAR1	Millipore	Cat# MAB363	10 µg/mL
antibody	Rabbit, Polyclonal, anti-GluA1-4, (pan-AMPA)	Dr. Elek Molnar /Bristol University	Generated by Dr. Elek Molnar	10 µg/mL
antibody	Goat anti-rabbit IgG conjugated gold particles	Nanoprobes Inc	#2003-0.5ML	(1:100)

recombinant DNA reagent	AAV5-CamKII-GFP-Cre	Penn Vector Core	AV-5-PV2521	Available on Addgene
recombinant DNA reagent	AAV5-CamKII-eGFP	Penn Vector Core	AV-5-PV1917	Available on Addgene
recombinant DNA reagent	AAV5-CamKII-mcherry-Cre	UNC Vector Core	See website	https://www med. unc.edu /genetherapy/ vectorcore/in-stock-aav-vectors/
recombinant DNA reagent	AAV5-CamKII-mcherry	UNC Vector Core-Dr. Karl Deisseroth Control Fluorophores	See website	https://www med. unc.edu /genetherapy/ vectorcore/in-stock-aav-vectors/
recombinant DNA reagent	AAV-DJ-flex-OChIEF-tdTomato	Dr. Pascal Kaeser PMID: **29398114**	Generated at UNC Vector Core	Custom Order
recombinant DNA reagent	AAV-DJ-DIO-BDNF-phluorin	Dr. Hyungju Park PMID: **25467984**	Generated at UNC Vector Core	Custom Order
chemical compound, drug	Ketamine	Merial	Cat#03661103001904	
chemical compound, drug	Xylazine	Calier	Cat#20100-003	
chemical compound, drug	Paraformaldehyde	Scharlau	PA0095	

chemical compound, drug	Glutaraldehyde	Electron Microscopy Sciences	Cat#16210	
chemical compound, drug	Picric Acid	Panreac	Cat#141048.1609	
chemical compound, drug	Phosphate Buffer	Scharlau	SO03321000	
chemical compound, drug	Human serum albumin	SigmaMillipore	A-1653	
chemical compound, drug	TBS: TRIZMA BASE TBS: Trizma HCl	SigmaMillipore	T1503 T3253	
chemical compound, drug	Triton X-100	SigmaMillipore	T8787	
chemical compound, drug	Polyethylene glycol	SigmaMillipore	25322-68-3	
chemical compound, drug	Uranyl acetate	Electron Microscopy Sciences	Cat#22400	
chemical compound, drug	Reynold's lead citrate	Electron Microscopy Sciences	#17800	
chemical compound, drug	Picrotoxin	SigmaMillipore	Cat# P1675	
chemical compound, drug	LY303070	ABX Chemical Co.	N/A	Custom Order
chemical compound, drug	MK-801	Tocris Bioscience	Cat# 0924	

chemical compound, drug	DCG-IV	Tocris Bioscience	Cat# 0975	
chemical compound, drug	D-APV	Tocris Bioscience	Cat# 0106	
chemical compound, drug	D-APV	NIMH Chemical Synthesis Program	N/A	
chemical compound, drug	R-CPP	Tocris Bioscience	Cat# 0247	
chemical compound, drug	NBQX	Cayman Chemical Co.	Cat# 14914	
chemical compound, drug	Fluo5-F pentapotassium salt cell impermeant	Invitrogen Molecular Probes	Cat# F14221	
chemical compound, drug	Alexa Fluor 594 Hydrazide	Invitrogen Molecular Probes	Cat# A10438	
chemical compound, drug	Alexa Fluor 488 Hydrazide	Invitrogen Molecular Probes	Cat# A10436	
chemical compound, drug	D-Serine	Tocris Bioscience	Cat# 0226	
chemical compound, drug	MNI-caged-L-glutamate	Tocris Bioscience	Cat# 1490	
chemical compound, drug	Sucrose	SigmaMillipore	Cat# S9378	
chemical compound, drug	KCl	SigmaMillipore	Cat# P3911	

chemical compound, drug	NaH_2PO_4	SigmaMillipore	Cat# S9638	
chemical compound, drug	$CaCl_2$	SigmaMillipore	Cat# C8106	
chemical compound, drug	$MgCl_2$	SigmaMillipore	Cat# M2670	
chemical compound, drug	$MgSO_4$	SigmaMillipore	Cat# M1880	
chemical compound, drug	Glucose	SigmaMillipore	Cat# G8270	
chemical compound, drug	NaCl	SigmaMillipore	Cat# S7653	
chemical compound, drug	$NaHCO_3$	SigmaMillipore	Cat# S6014	
chemical compound, drug	Cesium hydroxide	SigmaMillipore	Cat# 23204	
chemical compound, drug	D-gluconic acid	SigmaMillipore	Cat# G1951	
chemical compound, drug	EGTA	SigmaMillipore	Cat# E4378	
chemical compound, drug	HEPES	SigmaMillipore	Cat# H3375	
chemical compound, drug	Potassium gluconate	SigmaMillipore	Cat# G4500	

chemical compound, drug	MgATP	SigmaMillipore	Cat# A9187	
chemical compound, drug	Na_3GTP	SigmaMillipore	Cat# G0635	
chemical compound, drug	NMDG	SigmaMillipore	Cat# M2004	
chemical compound, drug	Sodium ascorbate	SigmaMillipore	Cat# A4034	
chemical compound, drug	Thiourea	SigmaMillipore	Cat# T8656	
chemical compound, drug	Sodium pyruvate	SigmaMillipore	Cat# P2256	
chemical compound, drug	$KMeSO_4$	SigmaMillipore	Cat# 83000	
chemical compound, drug	Na_2ATP	SigmaMillipore	Cat# A2383	
chemical compound, drug	NaGTP	SigmaMillipore	Cat# 51120	
chemical compound, drug	Sodium Phosphocreatine	SigmaMillipore	Cat# P7936	
chemical compound, drug	NH_4Cl	SigmaMillipore	Cat# A9434	
chemical compound, drug	KOH	EMD Millipore	Cat# 109108	

chemical compound, drug	HCl	Fisher Chemical	Cat# SA49	
software, algorithm	IgorPro7	Wavemetrics		https://www.wavemetrics.com/
software, algorithm	Origin Pro 9	Origin Lab		https://www.originlab.com/
software, algorithm	ImageJ	ImageJ		http://imagej.net/Welcome
software, algorithm	Multiclamp 700B	Molecular Devices		https://www.moleculardevices.com/
software, algorithm	Prairie View 5.4	Bruker Corp.		https://www.pvupdate.blogspot.com/

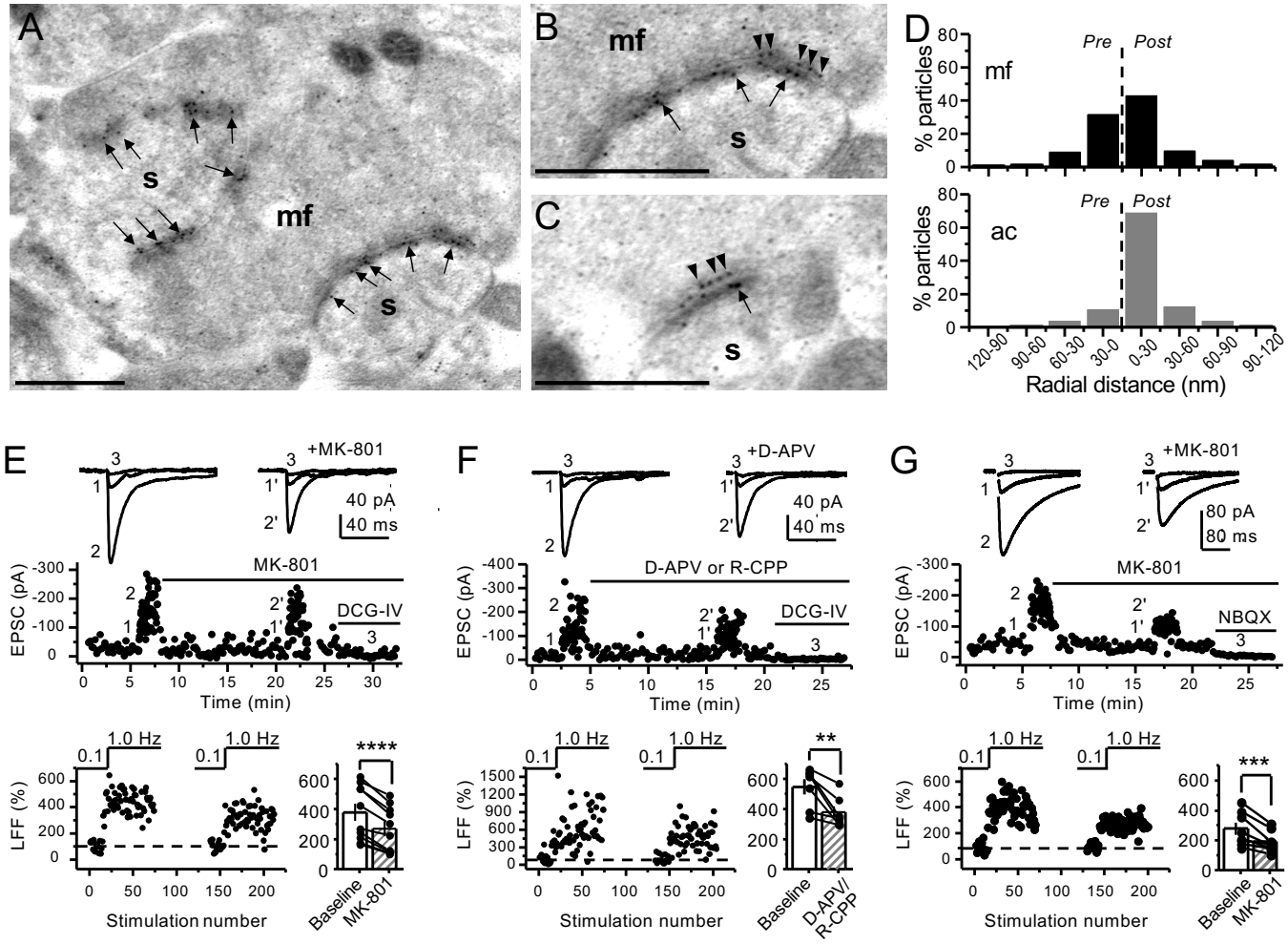

Figure 1. Anatomical and functional evidence for preNMDARs at mossy fiber synapses.

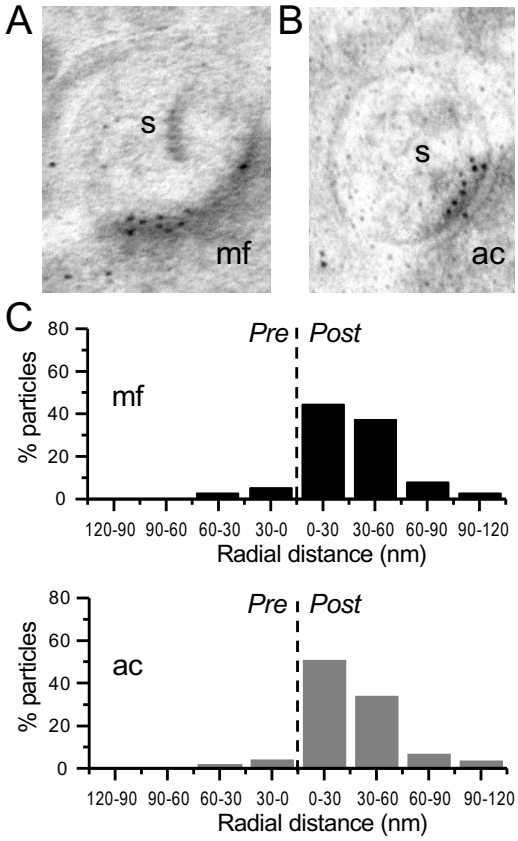

Figure 1-figure supplement 1

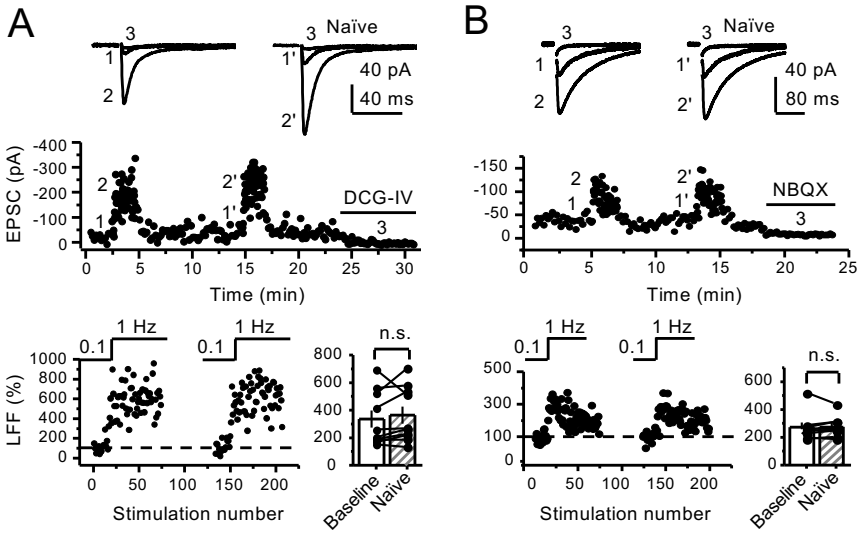

Figure 1-figure supplement 2

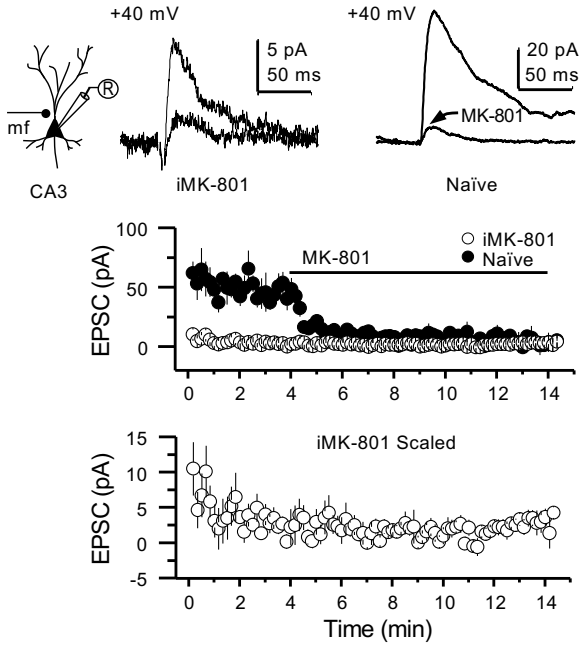

Figure 1-figure supplement 3

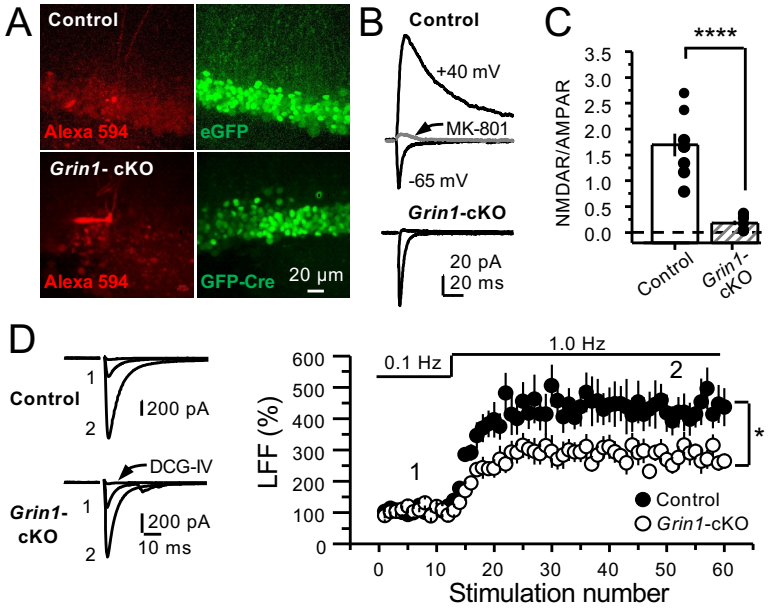

Figure 2. GluN1 deletion from granule cells reduces mf-CA3 facilitation.

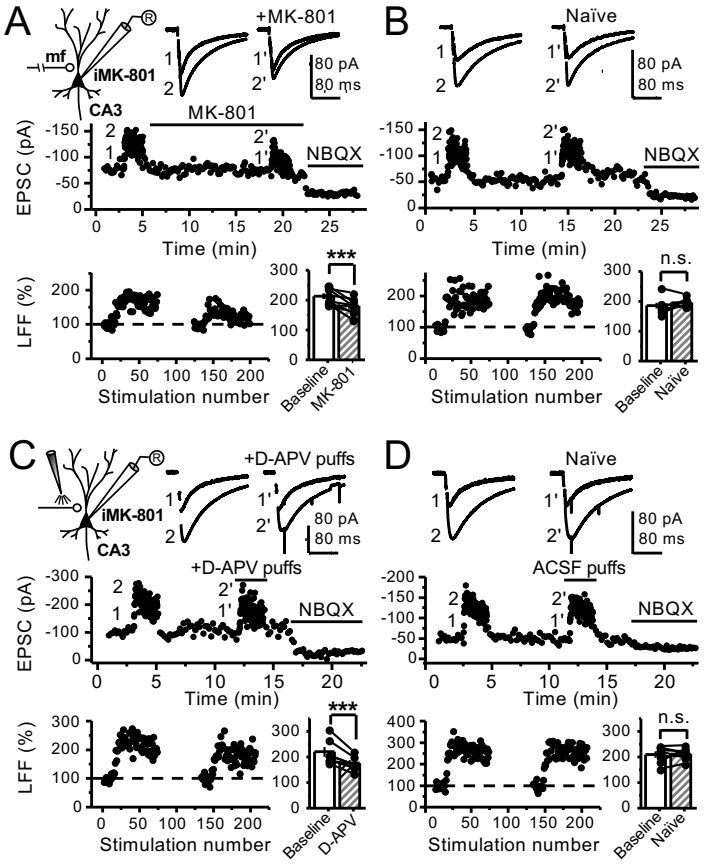

Figure 3. Reduced facilitation by NMDAR antagonism is independent of the GC somatodendritic compartment.

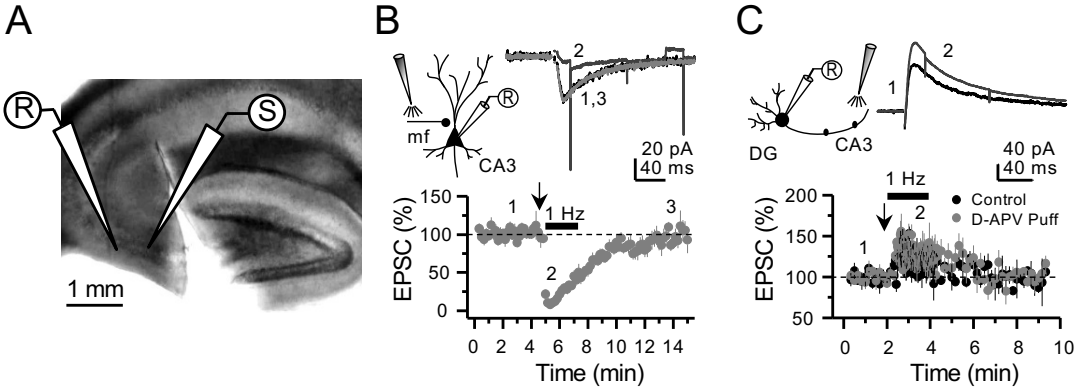

Figure 3-figure supplement 1

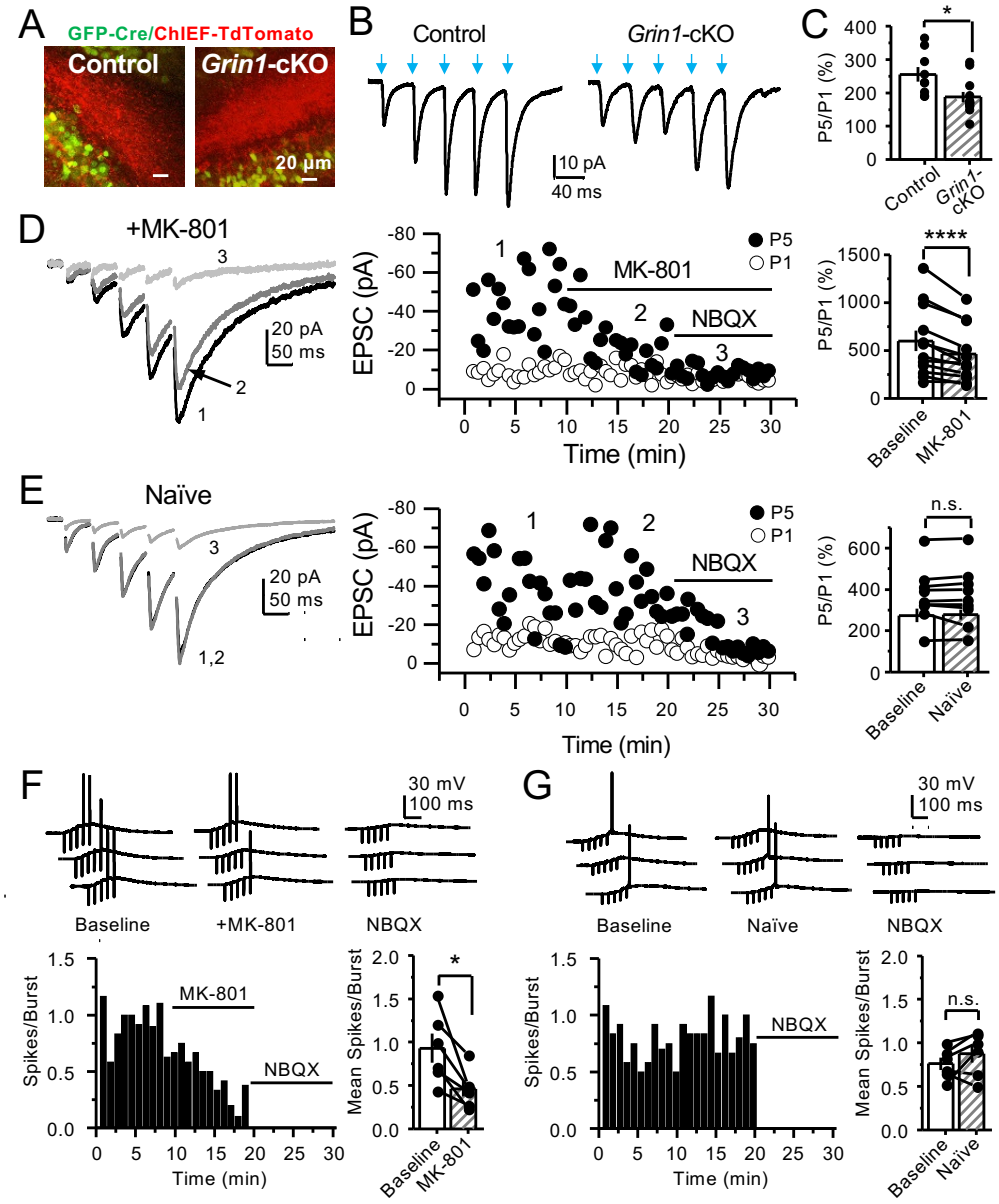

Figure 4. PreNMDARs contribute significantly to burst-induced facilitation and spike transfer.

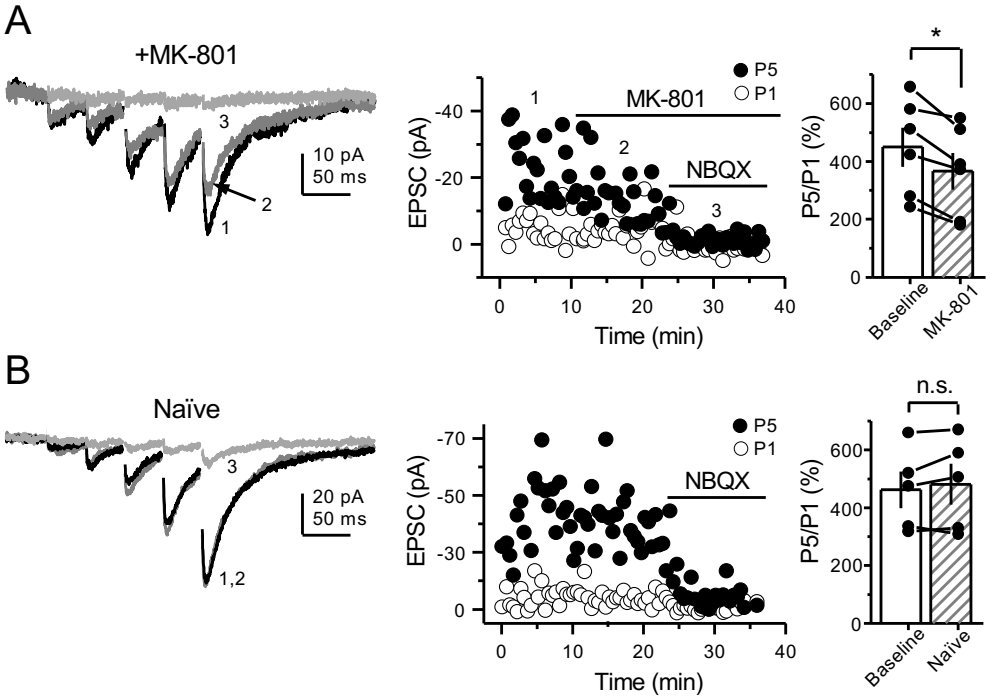

Figure 4-figure supplement 1

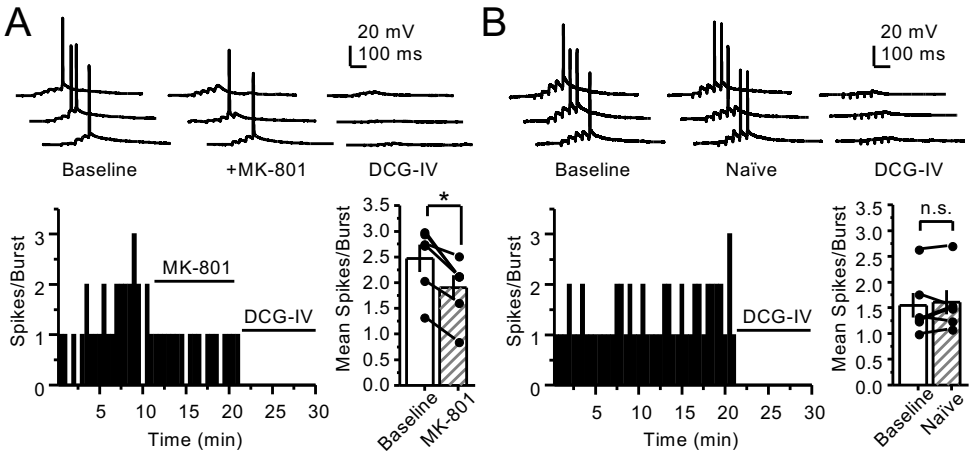

Figure 4-figure supplement 2

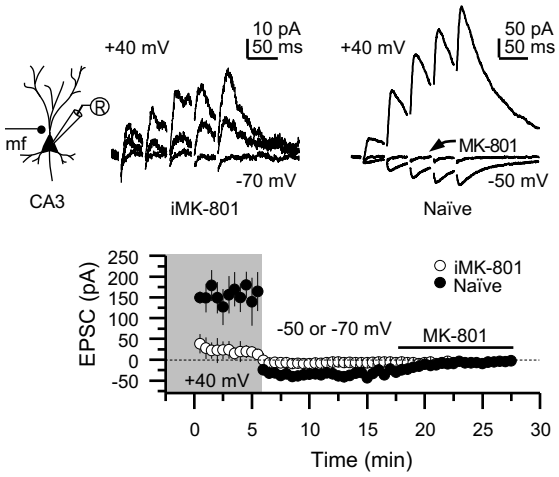

Figure 4-figure supplement 3

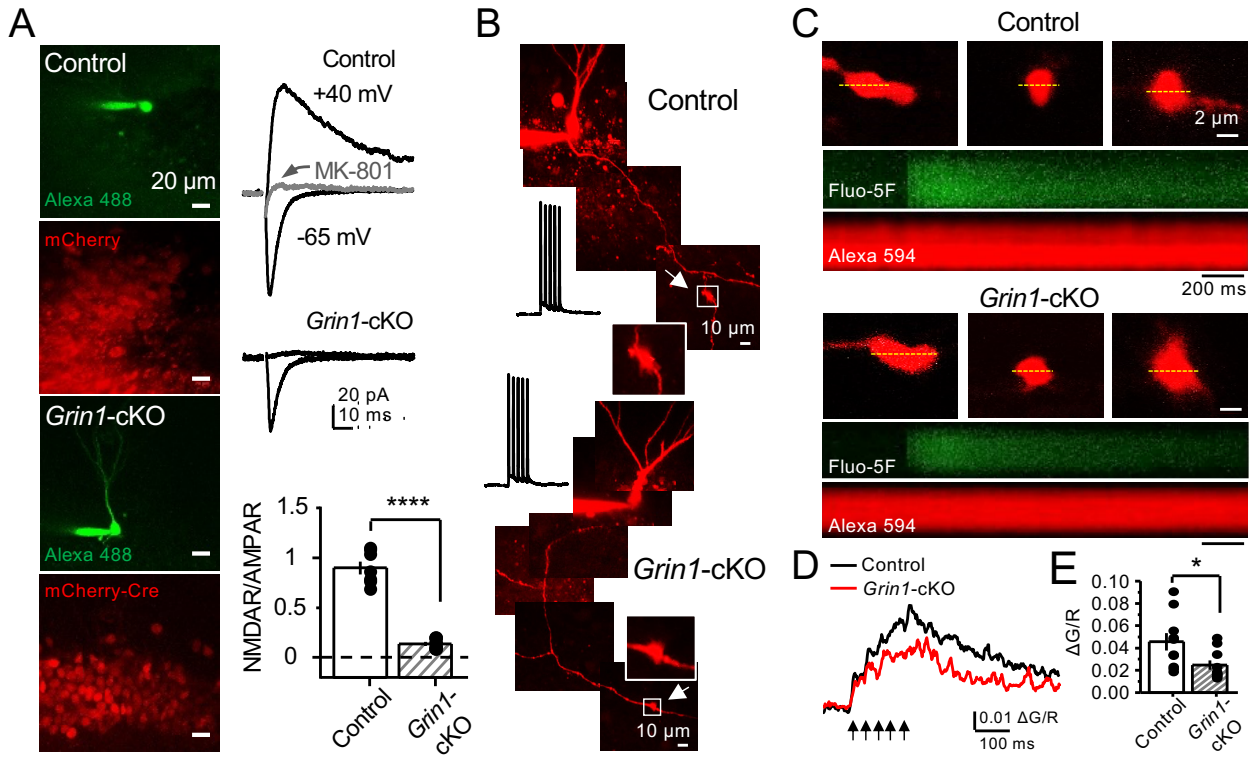

Figure 5. preNMDARs contribute to presynaptic Ca^{2+} rise.

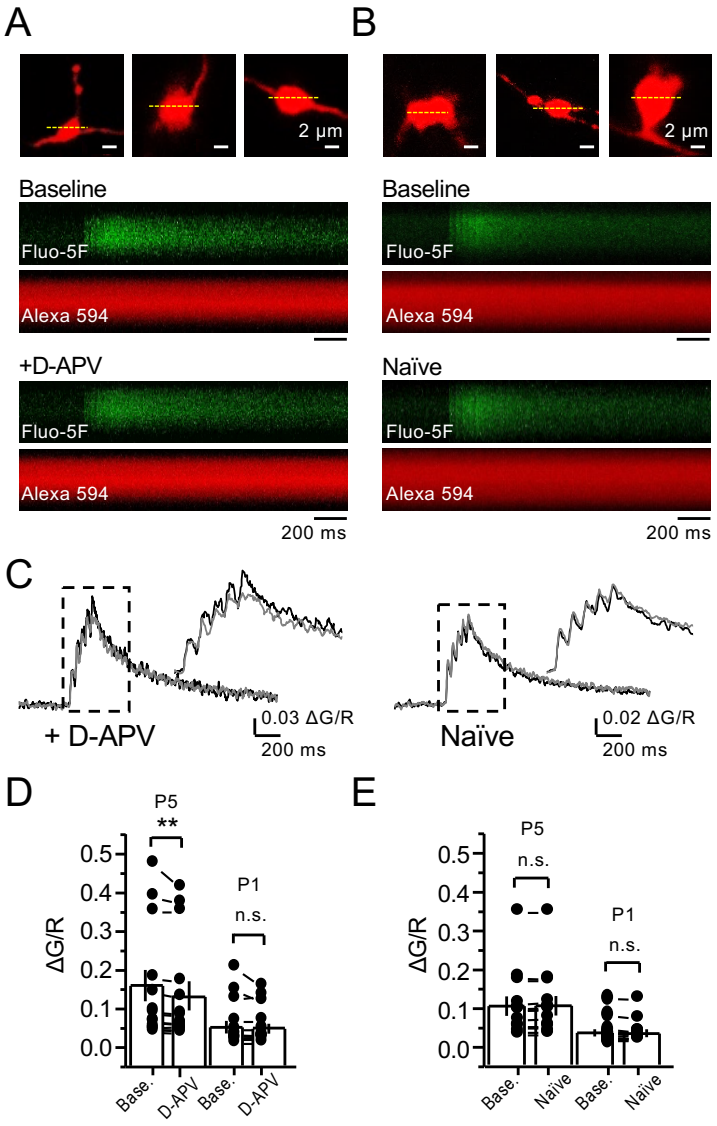

Figure 5-figure supplement 1

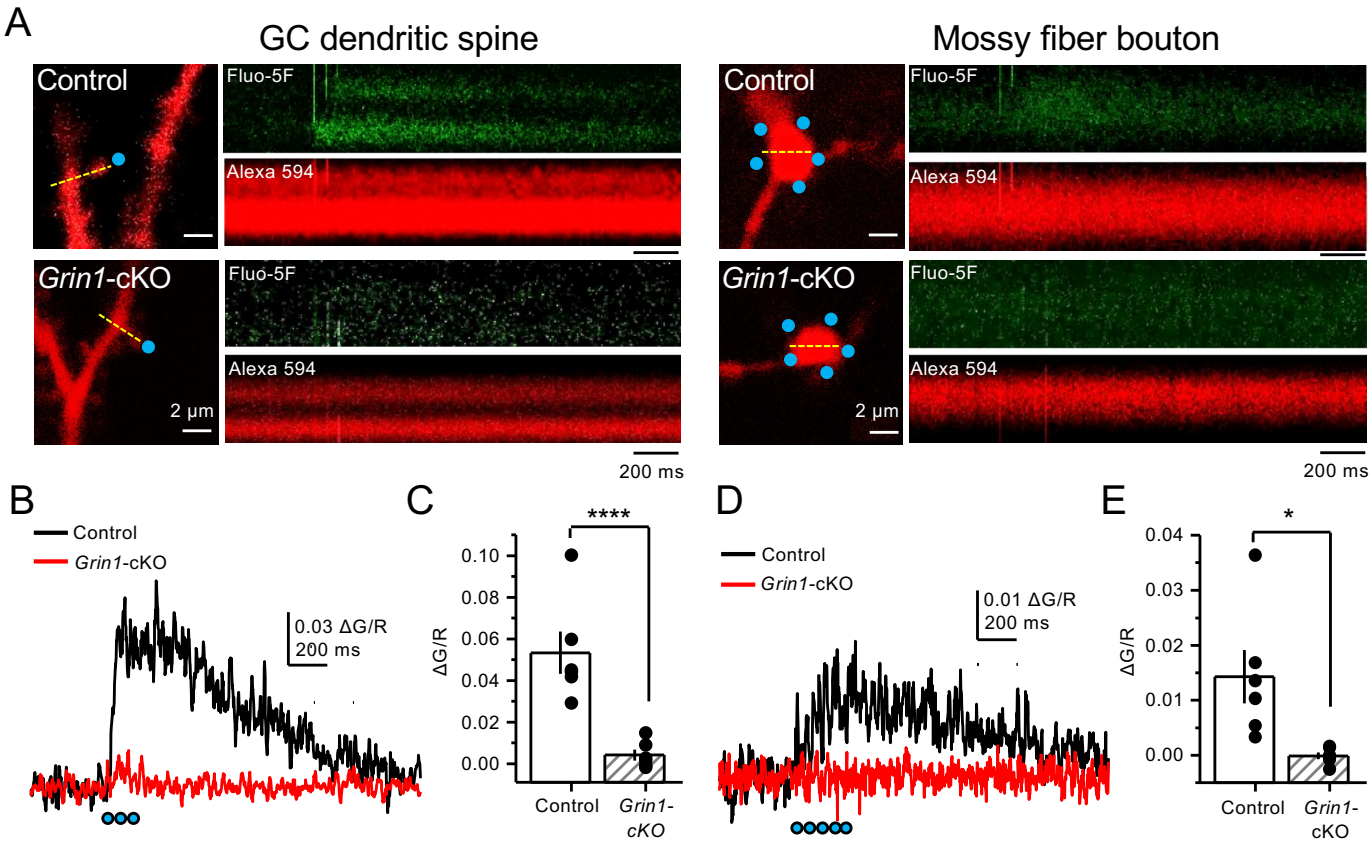

Figure 6. Uncaging glutamate induces Ca^{2+} rise mossy fiber boutons.

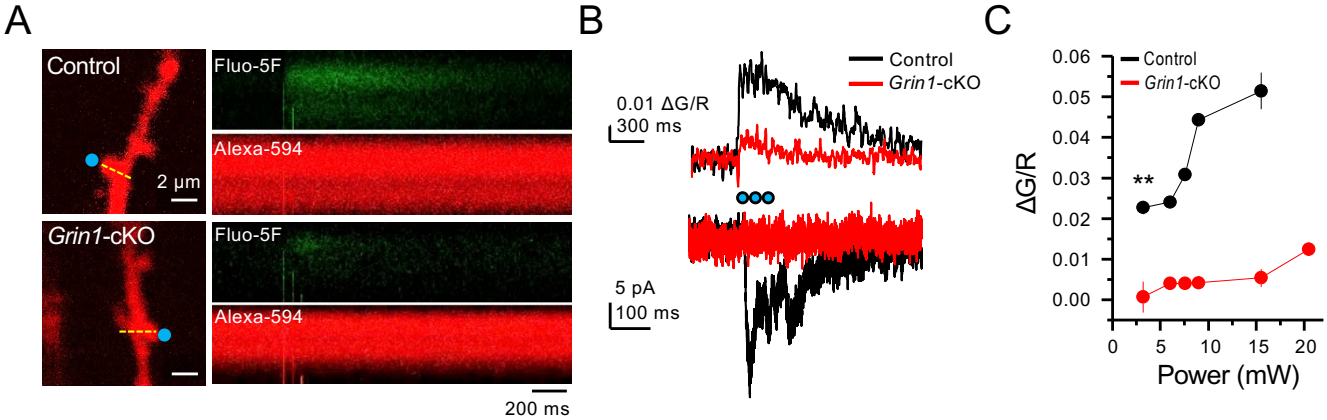

Figure 6-figure supplement 1

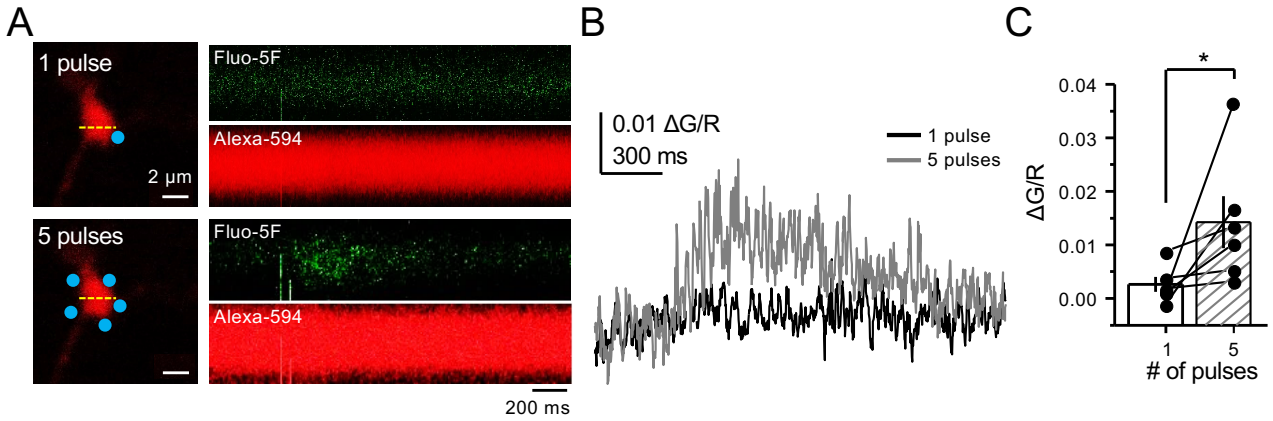

Figure 6-figure supplement 2

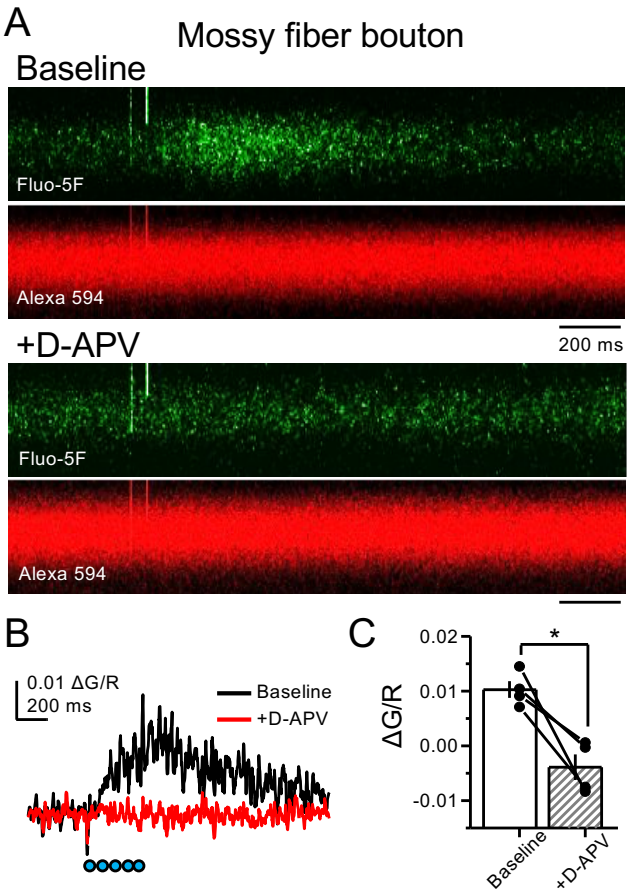

Figure 6-figure supplement 3

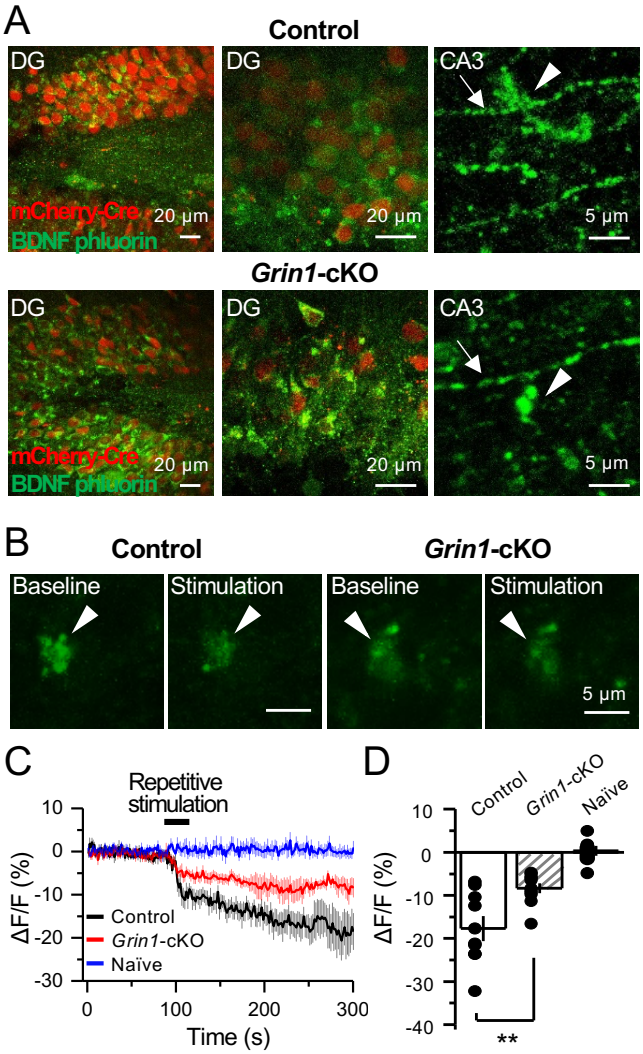

Figure 7. preNMDARs contribute significantly to BDNF release following repetitive activity.

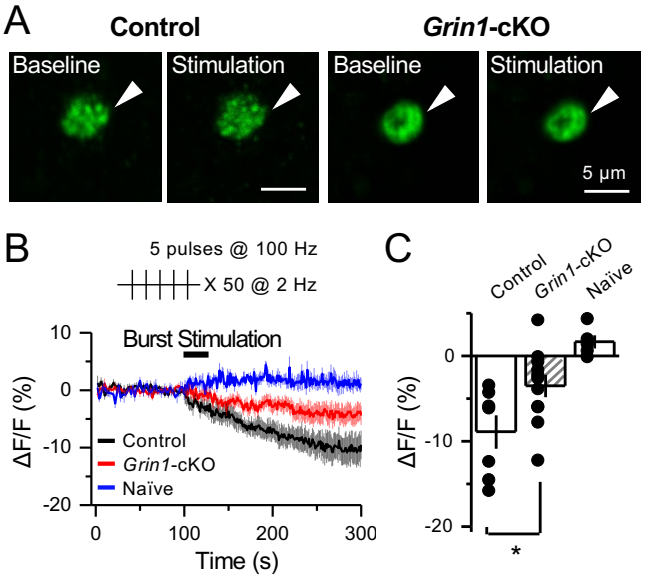

Figure 7-figure supplement 1

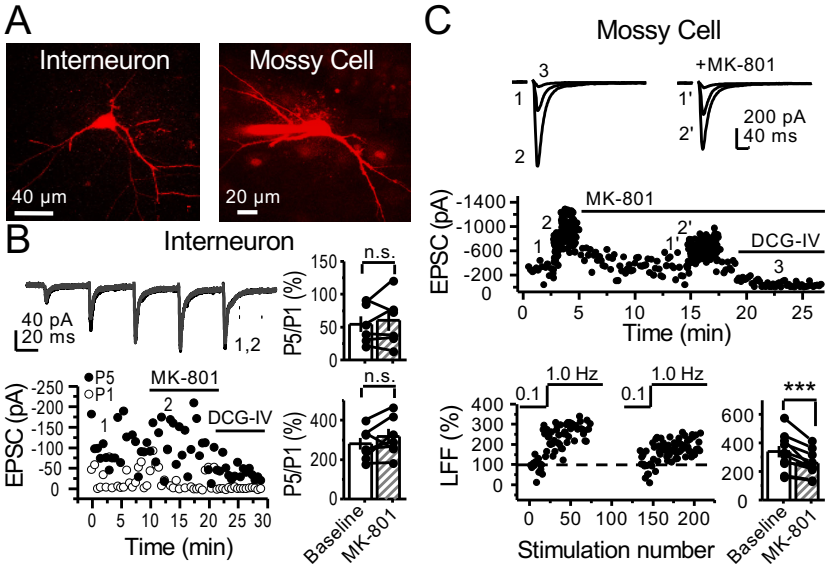

Figure 8. preNMDARs contribute to synaptic facilitation of mossy fiber inputs onto mossy cells but not onto CA3 inhibitory interneurons.

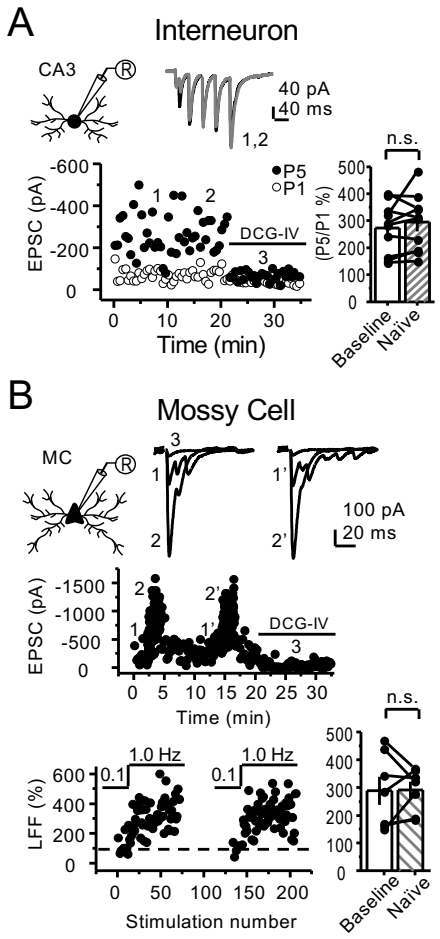

Figure 8-figure supplement 1